Three-dimensional Ca2+ imaging advances understanding of astrocyte biology

— Source link ⬈

Erika Bindocci, Iaroslav Savtchouk, Nicolas Liaudet, Denise Becker ...+2 more authors

Institutions: University of Lausanne

Related papers:

- Ca 2+ signaling in astrocytes from Ip3r2 –/– mice in brain slices and during startle responses in vivo

- Transient Opening of the Mitochondrial Permeability Transition Pore Induces Microdomain Calcium Transients in Astrocyte Processes

- Gliotransmitters Travel in Time and Space

- Astrocyte Calcium Signaling: The Third Wave

- Local Ca2+ detection and modulation of synaptic release by astrocytes

Author Manuscript

Faculty of Biology and Medicine Publication

This paper has been peer-reviewed but does not include the final publisher proof-corrections or journal pagination.

Published in final edited form as:

3D Ca^{2+} Imaging Advances Understanding of Astrocyte Biology

Erika Bindocci†, Iaroslav Savtchouk†, Nicolas Liaudet†, Denise Becker, Giovanni Carriero and Andrea Volterra*

Department of Fundamental Neuroscience, University of Lausanne, Rue du Bugnon 9, 1005 Lausanne, Switzerland

*Corresponding author E-mail: andrea.volterra@unil.ch

†These authors contributed equally to the study

Until today, astrocyte communication has been studied by 2D Ca^{2+} imaging, without producing conclusive data on the role of astrocytes in synaptic and vascular function. We developed a 3D two-photon imaging approach and studied Ca^{2+} dynamics in entire astrocyte volumes, including during axon-astrocyte interactions. In both awake mice and brain slices, Ca^{2+} activity in an individual astrocyte is scattered throughout the cell, including in gliapil, largely compartmented between regions, preponderantly local within regions, and heterogeneously distributed regionally and locally. Processes and end-feet display frequent fast activity, whereas soma is unfrequently active. In awake mice, activity is higher than in brain slices, particularly in end-feet and processes, and displays occasional multifocal cell-wide events. Finally, astrocytes respond locally to minimal axonal firing with time-correlated Ca^{2+} spots.

INTRODUCTION

Astrocytes translate information received from neighboring CNS cells and generate modulatory responses at local or network level via Ca^{2+} signaling(1-6). They show intracellular Ca^{2+} elevations in response to neuronal activity(7-10), which result in downstream effects on synaptic transmission and plasticity(11-15). Astrocytic Ca^{2+} elevations also trigger vascular responses, possibly involved in the control of cerebral blood flow(16-19). Therefore, deciphering the "Ca^{2+} language" of astrocytes is an essential step towards defining their role in physiological and pathophysiological brain function. Despite the potential importance, modalities and implications of astrocytic Ca^{2+} signaling are still not well understood. Perplexingly, in each domain in which some studies identified a specific role for this signaling(7, 11-15, 20, 21), others subsequently reported inconsistent results(22-26), casting doubt on the original observations and fostering controversy. A neglected aspect in astrocyte studies and a potential source of inconsistencies is the spatial limitation imposed by two-photon Ca^{2+} imaging. Even the most technically advanced studies so far monitored just small portions of total astrocytes, contained in a single 1D line or 2D plane, assuming that such portions were representative of the whole astrocyte Ca^{2+} activity. This is, however, dubious given the highly 3D nature of astrocytes and of their relations with neighboring vascular and neuronal elements as well as the emerging complexity of the astrocytic Ca^{2+} activity(2). Based on the reported potential feasibility of 3D two-photon Ca^{2+} imaging in astrocytes(27) and the recent availability of fast scanners and sensitive detectors, we tested 3D scanning of entire astrocytes. By selectively expressing the genetically-encoded Ca^{2+} indicator (GECI), GCaMP6f (28) in astrocytes, we succeeded in capturing whole astrocyte Ca^{2+} activity, including in structurally unresolved regions, the so-called gliapil. By combining expression of another GECI, jRCaMP1a (29) in neurons, we addressed synapse-astrocyte interactions. 3D monitoring generated tens of gigabytes of data per acquisition that we treated with a dedicated analytical framework developed in house, providing the first quantitative description of Ca^{2+} dynamics throughout a 3D astrocyte, in both brain slices and awake mice.

RESULTS

3

Comparing study of astrocytes in 2D and 3D

Astrocytes have been studied so far via two-photon microscopy in a single horizontal plane (2D imaging). To quantitatively compare their morphological study in 3D versus conventional 2D imaging, we initially performed morphometric analysis of astrocytes in hippocampal slices from *GFAP-EGFP* mice (see Methods; n=21, 7 from CA1, 6 from CA3 and 8 from dentate gyrus, DG). We acquired z-stacks containing the entire structure of individual astrocytes and extracted their morphology by software-assisted masks creation. Astrocytes appeared as structurally compact and optically resolved in their core regions (soma, stem processes with appendages ≥1 µm, end-feet), but "spongy" in their more peripheral regions, the gliapil, formed by fine branches and lamellae below optical resolution. Therefore, we extracted volumes directly from fluorescence measures in the structural "core", whereas we corrected measures done in the gliapil for volume fraction (see Methods). The estimated average volume of an astrocyte was 13'019±1750 µm³ (range 3'000–35'000 µm³), 25±2.5% of which was occupied by the structural core and 75±2.5% by the gliapil. Within the core, the soma occupied 22.5±2.2% of the volume, the stem processes with appendages 74±2.5%, and the end-feet 3.5±0.7%. On average, each hippocampal astrocyte had 3.5 end-feet (range: 1-7) and 5.8 stem processes (range: 3-9), and each process was 20.9 µm long (range: 5-64 µm) (Fig 1). Astrocytes of the CA1, CA3 and DG regions were not significantly different in their volume measures (P=0.76, 0.3, 0.3, for total, core and gliapil volume, respectively, Kruskal-Wallis test) and were, therefore, grouped in subsequent analyses.

Next, we quantitatively compared 2D with 3D studies. In particular, for a given astrocyte structure, we compared the structure volume visible in the best single two-photon focal plane (axial resolution: ~1µm; see Methods), to the total structure volume. A single two-photon focal plane reports at maximum 4.0±0.30% of the volume of a hippocampal astrocyte (Fig 1, Movie S1). The best plane for end-feet reports 21.9±2.79% of the calculated end-foot volume and contains at maximum 2 out of 3.5 end-feet; for soma, the best plane reports 10.44±0.60% of its volume, and for processes, 6.12±0.54% of their volume and contains 2.6 out of 5.8 processes, with an average length of 9.55 µm (range 1-41.9).

A 3D Ca²⁺ imaging and analysis approach for astrocyte studies

The above data call for developing a 3D approach to study astrocyte biology. We combined state-of-art technologies and new analytical methods (Fig. 2). For studying astrocyte Ca²⁺ dynamics, we generated double transgenic mice conditionally expressing GCaMP6f under GFAP promoter, i.e. *hGFAPCreERT2xGCaMP6f* mice (see Methods). Analysis of GCaMP6f-positive cells in hippocampal slices from *hGFAPCreERT2xGCaMP6f* mice stained with anti-GFP antibodies (Fig. S1), confirmed astrocyte-specific expression of GCaMP6f in both the CA1 and CA3 regions (100% of GFP-positive cells double-positive for the astrocyte marker, glutamine synthase, and 0% for the neuronal marker, NeuN). In the DG, expression was 90% in astrocytes and 10% in other cells, most likely immature and newborn granule cells. GCaMP6f expression was homogenous throughout the volume of individual astrocytes, including in the structurally unresolved gliapil region (Fig. S1C). Astrocytes were also live-stained with the Ca²⁺-independent dye, sulforhodamine 101 (SR101, 0.05-0.5 µM, see Methods). By combining SR101 and GcAMP6f maps, we obtained information for analysis of Ca²⁺ dynamics in both structurally resolved (core) and unresolved (gliapil) astrocyte regions, and could detect movement artefacts, notably *in vivo*. Our 3D imaging approach consisted in framing an isolated GCaMP6f-expressing astrocyte into a cuboid, the VOI, and in rapidly acquiring images from its territory at a routine rate of about 2Hz, i.e., of two full z-stacks (~60 focal planes) every second. Thanks to our advanced imaging apparatus (see Methods) and the high signal-to-noise ratio of GCaMP6f, at this speed we captured all the Ca²⁺ events with duration ≥1.5 sec (FWHM, full width at half-maximum amplitude) occurring in the selected VOI. Faster events (<1.5 sec) were visualized by increasing acquisition rate in more restricted volumes (Figs. S3,S5,S8). Each of our imaging acquisitions generated datasets of several gigabytes. For their treatment we developed two complementary analysis methods, one optimized for analysis of Ca²⁺ events in structurally resolved regions (see also (*14*)), and another for analysis of Ca²⁺ activity in the absence of structural information, therefore in both core and gliapil (Fig. 2 and Methods).

Distribution of Ca²⁺ dynamics in a 3D astrocyte and related problems of 2D imaging

At first, we quantitatively estimated the total Ca²⁺ activity in an entire astrocyte in basal condition. Activity detected during 3-minute-long acquisitions in hippocampal astrocytes in situ (P30-40; n=14 cells, 5 in CA1 and 9 in DG) and expressed as mean voxel frequency (see Methods; 17'310±1'591 voxels/astrocyte; voxel size: 1 µm³) was 9.20±1.34 mHz. Activity distributed analogously in structural core and gliapil, as the percentage of activity in each compartment broadly matched its percentage volume (gliapil: 80% of activity, 75% of astrocytic volume; core: 20% of activity, 25% of volume). Total activity did not change in a second run (P=0.43; signed rank test), indicating that, macroscopically, astrocytic activity is stable over time and not influenced by laser scanning. Next, we calculated how much of the total Ca²⁺ activity detected in 3D is reported by 2D imaging. We subdivided the 3D map of total Ca²⁺ activity in each astrocyte into a z-stack of 1 µm-thick lateral planes, representing all the focal planes available in a conventional 2D two-photon acquisition (Fig. 3A) and expressed the total activity in each plane as percentage of the total 3D activity. The best focal plane reported, at maximum, 11.4±0.8 % of the total activity of an astrocyte (Fig. 3B, Movie S2).

We then analyzed Ca²⁺ activity in the structural core of the astrocyte, where we could define and characterize individual Ca²⁺ events. Of 666 events detected during 3D acquisitions from 15 cells, 567 (85.2%) occurred in processes, 65 (9.7%) in end-feet and 34 (5.1%) in the soma (Fig. 3C and D; mean event features in Table S1). According to our estimations, 61% of such events would have been missed in conventional 2D imaging experiments, and the remaining 39% incorrectly reported (Fig. S2).

We next considered under-sampling of the Ca²⁺ activity. The 2Hz rate used here in 3D is within the range used in most 2D studies and represents the best compromise for imaging entire astrocyte activity with our system. Nonetheless, astrocytic activity was reported to also comprise fast events with FWHM ≤1.5 sec (*14,30,31*), not correctly captured at 2Hz. Therefore, in some experiments, we restricted the 3D sampling volume to increase acquisition speed. We selected VOIs of 8 focal planes centered on either an astrocytic process or one or multiple end-feet, including surrounding gliapil, and compared event detection at 2 and 10 Hz. Faster scanning captured more Ca²⁺ events, resulting in a 4.9-fold and 5.4-fold event frequency increase in processes (n=8 processes in 4 cells) and end-feet

6

(n=13 end-feet in 4 cells), respectively (Figs. S3,S5,S8). In particular, a new population of fast events appeared at 10 Hz (see below).

Distribution of Ca^{2+} dynamics in 3D astrocytes in awake mice

Next, we investigated astrocytes *in vivo*, in the somatosensory cortex of adult awake mice. Morphological analysis of the astrocytes in that region did not show any significant difference with respect to hippocampal astrocytes, except for a higher number of end-feet per cell, 5 (range 4-7) versus 3.5 (P=0.03; rank sum test; n=21 hippocampal cells, 6 somatosensory cortex cells). We then performed 3D Ca^{2+} imaging, combining simultaneous camera tracking of the mouse movements (Movie S3) and initially estimated the total Ca^{2+} activity in individual astrocytes. Mean voxel frequency was 22.73±2.74 mHz (n=9 cells, Fig 3C), significantly higher than in hippocampal astrocytes *ex vivo* (+147%; P=0.0002, Mann-Whitney test). This enhanced frequency was a feature of the *in vivo* condition, not of the brain area studied or of the age of the mice. Thus, in slices of 4-months-old mice, mean voxel frequency in somatosensory cortex astrocytes was 8.48±2.05 mHz (n=3 cells), i.e. significantly lower than *in vivo* (-63%; P=0.018), and analogous to the frequency in hippocampal slices of younger mice (P=0.99). High activity *in vivo* depended on the awake state, as activity in mice under isoflurane anesthesia dropped to 3.87±1.31 mHz (n=3 cells), only 17% of the activity of awake mice (P=0.009) and <50% of the activity in astrocytes of brain slices (P=0.028). Visually, activity in awake mice was high in both structural core and gliapil and occurred with faster dynamics than *ex vivo*. Thanks to motion correction (see Methods), we could count individual Ca^{2+} events in the structural core and further analyze part of them. Of 740 events detected in 9 cells, 543 involved the processes (73.4%), 176 the end-feet (23.8%), and 21 the soma (2.8 %). Their normalized frequencies, when compared to those *ex vivo* (see Methods), gave *in vivo/ex vivo* ratios of 3.18 for end-feet (P<0.0001, rank sum test), 1.82 for processes (P=0.0016) and 1.17 for soma (P=0.19, Fig. 3C).

3D Ca^{2+} activity in astrocytic processes

We then performed in-depth analysis of Ca^{2+} activity in the different core structures. We started with astrocytic processes in situ (n=72 processes from 14 hippocampal astrocytes).

Average activity was different in different processes, ranging from 0 to 14 mHz (mean voxel frequency, Fig. 4A), with 71% of processes showing low (0-3 mHz), 19% medium (3-6 mHz) and 10% high activity (>6 mHz). These levels were broadly stable in repeated acquisitions (Fig. S4A). In most astrocytes, combinations of poorly active and more active processes were observed (Fig. 4A). Moreover, different processes were differently sensitive to the neuronal activity blocker, TTX (1 µM): 48% of them showed strong Ca^{2+} event reduction (>75%), 24% only partial (25-75%), and 28% no reduction (n=21 processes in 5 cells, Fig. 4B). We then analyzed process activity in awake mice (60 processes from 9 cortical astrocytes). Overall, processes *in vivo* were more active than processes *ex vivo* (maximal process activity: 28 vs. 14 mHz), but, like them, showed heterogeneous levels of activity (12% had low activity, 37% medium activity, 52% high activity), and combinations of more and less active processes in the same astrocyte.

We next analyzed Ca^{2+} activity distribution within individual processes. By averaging data from 72 processes in situ, we extracted mean voxel frequency per process volume (Fig. S4B). In an "average process", the largest volume fraction (>40%) contains very low/no activity (≤3 mHz). As the activity increases, the volume occupied is less and less, reaching <1% at frequencies >30 mHz. This suggests the presence of small hot spots. Indeed, analysis of the 17 most active processes showed heterogeneous alternation of hot and cold spots along the processes (Fig. 4C,D). The "hottest" and "coldest" spots in a process were 1.5±0.3 and 2.2±0.31 µm-long, respectively, measured from activity maps calculated in 1-µm increments (see Methods). No evident trend for associating these spots to specific process regions emerged.

Part of the Ca^{2+} events generated in processes reached the border with the somatic region, defined by the 3µm-long sub-region that we segmented at the interface between the two compartments. Only 22% of such events crossed the border and invaded the soma, whereas 78% stopped at the border (n=98 events). A few experiments at higher acquisition speed (10 Hz) better delineated the characteristics of "crossing" vs "stopping" events (n=10 and 65, respectively, Fig S4C). Crossing events had longer duration (4.10 times, P=0.0019, unpaired t-test) and higher amplitude (1.52 times, P=0.048, unpaired t-test) than "stopping events" (n=7 and 21 events, respectively). Experiments at 10 Hz also confirmed that

process activity (n=216 events in 8 processes) is largely local (mean event size: 40.50±3.11 μm^3, corresponding to 12.49±1.11% of the process volume) and enriched in fast events (FWHM: 0.68±0.3 s), difficult to capture in 2Hz acquisitions (detailed analysis in Fig. S5).

3D Ca^{2+} activity in the somatic region

We then investigated the astrocytic Ca^{2+} events involving the somatic region in both hippocampal slices and awake mice. Analysis was restricted to events that could be correctly extracted (29 events from 14 cells in situ and 11 from 9 cells *in vivo*). For several events *in vivo*, severe pollution by movement-related out of focus during acquisition prevented correct parameters definition. In astrocytes of hippocampal slices, events involving the soma were highly heterogeneous and spread spatially over a vast range of volumes, from tens of μm^3 to ~3'000 μm^3 (Fig. 4E). Part of them were relatively small (≤300 μm^3), mostly confined to the soma itself or resulting from activity in a proximal stem process invading the soma, often just partially. Others were larger and expanded to the whole somatic region plus additional connected structures, such as part or all of one or multiple stem processes and surrounding gliapil. Volume of an event and its duration seemed to be related, with the largest events being also the longest-lasting ones (Fig. 4E). We never observed in slices a somatic event that spread throughout the astrocytic core. Events *in vivo* had faster kinetics and a larger range of volumes than events *ex vivo*, going from ~890 μm^3 to 10'000 μm^3 (average: 4470±1051 μm^3, Fig. 4E). Part of these events expanded to volumes similar to those of the largest events *ex vivo*, but others were much larger (mean volume: 6375±1106 μm^3, n= 7 events) and involved the whole structural core of the astrocyte and good part of the surrounding gliapil. We called this new class, the "global" events. They appeared to originate at several unrelated foci, generally in the gliapil, and from there to expand to the rest of the astrocyte (Figs. 4F, S6). 6/7 global events occurred in temporal correlation (delay of onset: 1-3 s) with the animal locomotion (Movie S3). In anesthetized mice lacking locomotion, they were not observed. If global events depend on intense neuronal discharge associated to movement (*32*), it seems logical that we did not see them in hippocampal slices displaying only sparse neuronal firing (*14*). To artificially increase neuronal discharge in the slices, we applied the pro-epileptogenic drug 4-aminopyridine (4-AP, 100 µM) and monitored local field potentials (LFPs) while

performing 3D Ca^{2+} imaging in astrocytes (see Methods). Within 10 min, 4-AP induced a regular series of large LFPs, representing events of hypersynchronous neuronal discharge (*33*). In temporal correlation (delay: ≤ 2 sec), we always observed a "global-like" Ca^{2+} event in the monitored astrocyte, much larger than all the somatic events recorded in basal conditions ($3'099\pm296$ μm^3, n=7; Fig S7).

3D Ca^{2+} activity in end-feet and related processes

We next analyzed the Ca^{2+} activity involving astrocytic end-feet. SR101-based segmentation revealed the presence of multiple end-feet per astrocyte, although sometimes we could hardly define their exact borders and number. To obtain more precise morphological information we performed parallel studies in fixed slices of *GFAP-EGFP* mice labelled with the end-foot-selective marker, Aquaporin-4 (AQP-4; Fig. 5A). Often two end-feet, stemming from different processes or from two branches of the same process, enwrapped contiguous segments of the same blood vessel. Less frequently, two end-feet enwrapped non-contiguous segments, or segments of two different vessels. Rarely ($\leq 20\%$ of cases), two end-feet were fully contained in a single focal plane.

Functional analysis was performed on 86 Ca^{2+} events from 17 astrocytes *ex vivo* and 174 events from 9 astrocytes *in vivo*. Despite the much higher frequency *in vivo* (Fig. 3C), events in the two conditions displayed similar spatial spread: the majority stayed confined to the end-foot domain itself (62% *ex vivo*; 53% *in vivo*, Fig 5C), whereas others involved both end-foot and connected process (35% *ex vivo*, 24% *in vivo*). Events expanding beyond the end-foot process were just 3% *ex vivo*. They reached 22% *in vivo*, but mostly as part of global astrocytic events. In a few recordings at 10 Hz with VOI centered on end-feet, we observed an additional population of events (Fig. S3). They were fast (FWHM: 0.75 ± 0.03 s) and highly spatially restricted, occupying just fractions of the segmented end-feet (on average $16.32\pm1.50\%$ of a single end-foot volume) (96/136 events in 13 end-feet, see Fig. S8 for detailed analysis).

Simultaneous monitoring of activity in two or more end-feet showed preponderant asynchronicity (81% of cases *ex vivo*; n=52 events; 58% *in vivo*; n=92 events, Fig. 5B). Enhanced synchronicity *in vivo* was mainly because of global events, which in fact coordinate all the astrocytic Ca^{2+} activity, not only end-foot activity. Another, more local

10

type of synchronicity involved two end-feet enwrapping contiguous segments of the same blood vessel and their associated end-foot processes (Fig. 5B). According to current views, end-foot processes should form a "functional unit" with related end-feet. Thus, they would function as "axon-like highways", conveying all the network-related information sensed by an astrocyte to their end-foot for coordinate control of local blood flow (*5*). Contrary to this, end-foot processes and related end-feet were often independently active, and only in 23% of cases *in vivo* and 30% *ex vivo* showed coordinated activity. Moreover, end-foot processes displayed mostly local activity, not different on average from that in other processes (mean voxel frequency other processes vs end-foot processes: *ex vivo*: P=0.32; *in vivo*: P=0.83, rank sum test).

3D imaging reveals local axon-astrocyte functional interactions

Next, we investigated the structural and functional 3D relations between axons and astrocytes in hippocampal slices from adult mice. For morphological studies, we virally injected the red reporter tdTomato in neurons of layers II-III of the entorhinal cortex (EC) of *GFAP-EGFP* mice (Fig. S9, Movie S4); for functional studies, injections were made in *GFAPCreERT2xGCaMP6f* mice. Thereby we highlighted a dense meshwork of fluorescent axons corresponding to medial and lateral perforant path (PP) fibers (Fig. 6A). Such fibers contain recurrent varicosities (interdistance: 3-20 µm) making excitatory synapses mainly onto dendritic spines of granule cells (GCs) in the outer two-thirds of the dentate molecular layer (*34*). PP axons did not keep horizontal trajectories along their paths, rather they deviated significantly both laterally and vertically (see Fig. 6B) and crossed astrocytic territories in a highly 3D manner. Reconstruction of five such axons artificially aligned at the starting point of the monitored tract, shows that axon-astrocyte interactions are comprehensively captured by 3D but not conventional 2D scanning (Fig. 6B). Therefore, 3D Ca^{2+} imaging is appropriate to answer whether astrocytes respond to minimal axonal stimulation, as reported by some studies (*14, 15*) and contradicted by others (*24, 26*). In order to address this question, we selected an axon stimulation protocol known to evoke minimal synaptic activation in dentate GCs (*14, 35*). The protocol consisted of a ramp of 1 to 5 pulses of 30 µA current delivered at 50 Hz, spaced by 20 sec intervals to avoid induction of any synaptic plasticity. Sometimes at the end we applied a tetanic stimulation

11

(100 pulses at 100 Hz) to assess maximal response. To visualize PP axonal activity and confirm minimal stimulation, we virally transfected layer II-III EC neurons with the red Ca^{2+} indicator, jRCaMP1a (29). Fluorescent PP axons were focally stimulated via the tip of a Quantum Dot-coated patch-pipette (QD pipette, 540 nm; see Methods; Fig 6C) and Ca^{2+} activity monitored in a VOI traced along the visible axonal fiber tracts proximal to the QD pipette. The above protocol elicited a series of distinct Ca^{2+} signals with peaks of increasing amplitude proportional to the number of pulses in the ramp (Fig. 6C). Even single pulse stimulations, representing individual action potentials, produced a jRCaMP1a signal in the axons. Repetition of the ramp at 20s intervals induced a highly reproducible pattern of small axonal Ca^{2+} responses, which were abolished in TTX (1 μM). Tetanic stimulation at the end of the ramp produced a Ca^{2+} signal of much higher amplitude (Fig 6C).

We then examined the astrocytic responses to such stimulations. We selected a tdTomato-fluorescent axon passing in the territory of a GCaMP6f-expressing/SR-101-loaded astrocyte (Fig. 7A and Fig. S9C for technical detail) and positioned the stimulating QD pipette proximal to it and ≥40 μm away from the astrocytic territory to avoid any direct astrocyte activation. We applied minimal axonal stimulation protocols spaced by no stimulation intervals (2-3 min) and simultaneously recorded Ca^{2+} activity throughout the 3D astrocyte volume (Fig. 7A,B; n=12 experiments). By using post-hoc cumulative cross-correlation analysis (see Methods), we identified the Ca^{2+} activity time-locked to axonal stimulation in the midst of all the endogenous astrocytic activity, and could build 3D maps of the astrocytic regions displaying axonal firing-related activity. We called these regions "reliably responding regions" because they consistently responded to all the stimuli in the protocol, even to the single pulses (Fig. 7A).

Often minimal in size (60.7±24.3 μm^3, Fig. 7B), responding regions were generally positioned in the gliapil, in direct vicinity of the visible axon targeted with the stimulation pipette. In some cases, they were also at some distance, possibly due to concomitant stimulation of non-fluorescent axons. To verify the extent of overall axonal recruitment (fluorescent and non-fluorescent fibers) we monitored post-synaptic Ca^{2+} responses evoked by our minimal stimulation protocol in GCs (n=3; Fig S10, also for methodological detail). Responses were confined to a minimal fraction of the monitored neuropil volume,

consistent with recruitment of a very limited number of axon fibers. Stronger stimulations activated a much higher neuropil fraction (Fig. S10D).

To verify robustness of our method for detecting astrocyte "responding regions" we performed several controls: (a) random selection of VOIs in the astrocytic territory equaling in size "responding regions" and check of their Ca^{2+} activity during the same acquisition period. Total activity in these VOIs was less than in "responding regions" and mostly time-uncorrelated with axonal stimulations (Fig. 7A,B; we called these regions "non-responding regions"); (b) within "reliably responding regions", comparison of Ca^{2+} activity during equal periods of stimulation and non-stimulation. Activity largely clustered in the stimulation periods (Fig. S11); (c) evaluation of TTX-sensitivity of the astrocyte Ca^{2+} activity in "responding" and "non-responding" regions. TTX suppressed Ca^{2+} activity only in "responding regions" ($-81\pm5.8\%$; $P<0.05$, sign rank test; n=6 experiments; Fig 7B, S11C).

Finally, to directly demonstrate the cause-effect relation between axonal firing and astrocytic Ca^{2+} activity in responding regions, we performed dual-color GECI 3D Ca^{2+} imaging and succeeded in a few experiments in monitoring simultaneously jRCaMP1a signals in axons and GCaMP6f signals in contiguous astrocytic regions (n=3). Fig. 7C shows temporally enlarged traces from one such experiment. A number of Ca^{2+} elevations are seen in the selected astrocytic region directly contiguous to the stimulated axonal fibers, each one time-correlated to the action potential-evoked axonal Ca^{2+} response present in the vicinity. Astrocytes responded even to the lower levels of stimulation in the ramp, including a single action potential pulse, although not all the axonal Ca^{2+} elevations were accompanied by an astrocytic Ca^{2+} elevation, possibly because of synaptic failures associated to minimal stimulation (*14*). Both axonal and astrocytic Ca^{2+} elevations were blocked in TTX, directly demonstrating the action potential-dependent origin of the local astrocyte responses.

DISCUSSION

We here studied astrocyte Ca^{2+} dynamics in 3D, capturing all the Ca^{2+} activity in the volume of an astrocyte, including in response to axonal firing. Several aspects permitted this advance: (a) the capacity to map Ca^{2+} dynamics throughout the astrocyte, in both

structurally resolved (core) and unresolved (gliapil) regions, in brain slices and *in vivo*, thanks to the combined use of an activity-independent indicator (SR101) delineating astrocyte morphology and controlling for movement artefacts, and a GECI (GCaMP6f) with high SNR and cell-wide, astrocyte-specific expression; (b) the capacity to scan the whole astrocytic territory at a routine rate of 60 different focal planes/sec capturing all astrocytic Ca^{2+} events with duration ≥ 1.5 sec, and to scan smaller, but functionally relevant, 3D domains (a process, one or multiple end-feet) at 5-fold higher rate to also capture faster events (<1.5 sec); (c) the capacity to study local 3D axon-astrocyte interactions, including with dual-color GECI imaging, and to resolve fine details of the respective activities, down to single action potential-related axonal Ca^{2+} transients and associated astrocytic Ca^{2+} spots; (d) the capacity to analyze datasets of tens of gigabytes per acquisition via in-house methods optimized for analysis of Ca^{2+} activity in the presence or absence of structural information.

3D imaging shows that Ca^{2+} activity is present throughout the astrocyte, including in structurally-unresolved regions and occurs mainly as a myriad of asynchronous local signals. The majority resides in the gliapil, which we estimated occupies ~75% of the cell volume. Within the smaller structural core, astrocytic processes are the region where Ca^{2+} activity is most frequent, followed by end-feet, particularly *in vivo*, whereas activity in the soma is infrequent (at least 20-30-fold less than in processes, see below). Passage of signals from region to region seems to be limited, possibly by barriers favoring regional compartmentation. Even within individual compartments, such as cell processes, activity is highly heterogeneous, and its level often differs significantly from process to process. Likewise, within individual processes, where hot and cold spots alternate.

3D imaging is not only appropriate but also necessary for correct study of Ca^{2+} dynamics in astrocytes. To start, astrocytic Ca^{2+} activity is highly heterogeneous and mostly local, clearly indicating that "partial imaging" of an astrocyte, as necessarily done in 2D studies, is not representative of the whole cell activity. According to our volumetric calculations, conventional 2D two-photon Ca^{2+} imaging covers no more than 4% of the astrocyte volume and 11% of its activity (with confocal imaging, focal volume may be set larger by opening the pinhole, but still minimal compared to the total astrocytic volume). Likewise, 2D

measures of activity in single astrocytic processes cannot be generalized to other processes, as simultaneous imaging of the different processes of an astrocyte shows differences in their activities as big as 20-fold. Partial imaging in 2D often reports incompletely even individual Ca^{2+} events. Thus, events detected in a single horizontal plane are not necessarily restricted to such plane, and assuming that they are, will often lead to erroneous description of their frequency and spatio-temporal characteristics (see Fig. S2). Finally, PP-axon-astrocyte interactions are highly 3D and unlikely to be correctly studied in 2D, particularly at low levels of axonal activity. Thus, astrocyte responses to minimal axonal stimulations appear as spot-like Ca^{2+} elevations that occupy <1% of their volume and would be missed with 2D imaging, unless by chance they occurred in the selected focal plane. This observation could explain why some previous 2D studies could not detect astrocyte responses to low levels of axonal activity and concluded that astrocytes respond only to intense neuronal firing(*26*). The latter responses are much larger in volume (e.g., Fig. S7, S11C) and likely to be seen in any randomly selected focal plane.

By performing 3D recordings in astrocytes from both brain slices and awake mice, we could directly compare the two conditions. Activity *in vivo* was faster and more frequent than in slices, but not crucially different in nature (mostly local and asynchronous) and cell distribution (mostly in processes, then in end-feet, and eventually in soma). Quantitatively, the most striking difference was the 3-fold higher frequency seen in end-feet. Qualitatively, the presence of a population of very large events, that we called "global" Ca^{2+} events, spreading to most of the astrocytic structures, including both core and gliapil. Most of these events were seen upon movement of the mouse and could be part of the widespread, multi-region astrocytic activation associated to the startle response(*36*). Global events were not spontaneously present in brain slices most likely because of the severing of projection fibers. Nonetheless, we could evoke global-like responses in slices by intensifying neuronal firing artificially, via 4-AP administration or high-frequency stimulation. Use of isoflurane anesthesia reduced astrocytic activity *in vivo* dramatically, down to levels much lower not only than in awake mice (-85%) but also than in brain slices (-55%), questioning the study of astrocyte biology *in vivo* in anesthetized mice.

An emerging feature of astrocytic Ca^{2+} activity is compartmentation. Only a tiny minority of the events seen in processes invaded the somatic region, and most of those that reached the interface stopped there. Likewise, for end-foot events: only a minority of them expanded to the related process and even less beyond it. This implies that some form of physical and/or biological barrier is present at the interfaces, such as a high concentration of buffering organelles or of soluble buffers operating like Ca^{2+} sinks. Local barriers could be present also within compartments and account for the observed alternation of hot and cold domains. In this respect, different astrocytic regions seem to differ in their resting Ca^{2+} level(37), and mobile mitochondria to operate along astrocytic processes as local Ca^{2+} buffers((38), but see(39)). Overall, an astrocyte could preponderantly function as an assembly of thousands of independent local units heterogeneously distributed both macroscopically and microscopically. Such heterogeneity could explain for example the different levels of activity observed in different processes of an astrocyte, or in different domains of an individual process, and their stability over time. While the underlying biological substrate remains to be defined, it might involve specific characteristics of the local microenvironment, including location and density of contacts with synapses; of receptors, channels and other proteins starting Ca^{2+} signaling; of internal organelles acting as Ca^{2+} sources and sinks. Functional units coordinate under specific circumstances, first more locally, and then more macroscopically. Multi-compartmental Ca^{2+} events are rather infrequent, and probably need to possess "supra-threshold" characteristics to cross interfaces and carry information requiring inter-compartmental coordination.

Most previous studies selected the soma as "reporter ROI" of the astrocytic Ca^{2+} activity, without knowing the exact nature and relative frequency of the phenomena involving this region. Via 3D imaging, we captured somatic Ca^{2+} events in their entirety and defined their relative frequency. Such events are very heterogeneous and cannot be considered a single family, as often done until now. Some of them are rather local, generated within or around the soma, and occupy only part of its volume; others are larger, and occupy the whole soma together with variable proportions of the astrocytic arborization; global events are even larger. These latter seem actually to be composite events originating at multiple independent foci, which variably contribute to their overall spatio-temporal expansion (Figs. 4F, S6). Even regrouping all these heterogeneous events, total somatic activity

remains very infrequent compared to activity in other compartments, counting for <3% of the total core activity recorded *in vivo*, and 5% of the activity *ex vivo*. These figures may actually overestimate the somatic contribution, as in high-speed recordings we captured additional fast activity in processes and end-feet. Therefore, somatic Ca^{2+} measures do not represent correctly the astrocyte biology, and are likely to lead to misinterpretations when pretending to address interactions of astrocytes with synapses and blood vessels, which may largely occur on a local basis and via fast events. This aspect needs to be highlighted because, even recently, influential studies interpreted major issues in astrocyte biology, like the existence or not of gliotransmission, based only on somatic Ca^{2+} measures(*23*) .

Ca^{2+} activity in end-feet was also preponderantly local, detached from the rest of the astrocyte including from end-foot process activity, and confined to individual end-foot domains, even to their fractions. Two or more end-feet, monitored simultaneously in different focal planes, were most of the times active independently, even when enwrapping contiguous segments of the same blood vessel. From time to time they underwent local coordination involving also the respective processes, possibly in response to a local vascular input(*40*) or to local synaptic activity. These observations are in line with recent data showing that neuronal activity induces fast Ca^{2+} signals in end-feet but not in the soma of astrocytes. These fast end-foot signals precede the vascular response and could be involved in neurovascular coupling(*20, 21*). We observed also a more general level of coordination *in vivo,* when global Ca^{2+} events coordinated the whole astrocyte. Such events have been associated to the slow component of the BOLD fMRI signal and would mediate a persistent vascular response to elevated neuronal activity(*41*).

Finally, we addressed presently debated issues concerning the "responsivity" of astrocytes to neuronal activity, i.e., whether astrocytes sense only high levels of neuronal activity(*26*) or also low levels(*14,15*), and whether their basal Ca^{2+} activity is in part neuronal activity-driven(*11-14*) or all intrinsically generated by the astrocytes(*26,39,42*). By scanning whole astrocyte volumes during axonal stimulations, we identified small local Ca^{2+} elevations time-correlated to minimal axonal activity, often spatially contiguous to the 3D trajectory of the visible active axons. Such astrocyte Ca^{2+} spots were TTX-sensitive and already detectable in response to a single action potential pulse, strongly supporting the view that

astrocytes sense even the lowest levels of neuronal activity. 3D imaging permitted also to identify a TTX-sensitive component of the basal Ca^{2+} activity in the processes of astrocytes in hippocampal slices, which distributed unevenly among different processes. This heterogeneity offers a reason why some previous 2D studies, which necessarily focused on individual, randomly-selected, processes, may have missed or underestimated this component (further discussion in Text S1).

In conclusion, our study shows that 3D Ca^{2+} imaging of entire astrocytes is possible and generates more complete and accurate information than any other approach previously used to study astrocyte Ca^{2+} dynamics. The present data provide plausible answers to several debated issues in astrocyte biology and new strategies to solve pending ones. They also highlight future challenges. For example, large part of the astrocytic Ca^{2+} activity, including fast components of global events and focal responses to neuronal firing, is located in the gliapil, i.e., outside the optically resolvable astrocytic structure. This calls for inclusion of detailed gliapil studies in future investigations. However, correct reporting of gliapil Ca^{2+} activity is beyond current technology. Only advanced super-resolution techniques will allow to resolve the fine gliapil structures, a step necessary to link signals to loci and investigate the underlying biology. New Ca^{2+} indicators capable of reaching adequate concentration in the low volume structures without causing excessive Ca^{2+} buffering will be also required. Additional technical challenges come from the nature of the astrocyte Ca^{2+} signals, mostly fast, local and scattered throughout the astrocytic territory. Only ultrafast scanning of entire astrocytes will permit proper capture of the whole gamut of signals. Here too current technology is limited, imposing a compromise between scanned volume, speed, and laser power deposited to the cell. In spite of these challenges, the 3D nature of astrocytes and of their local interactions with synapses and blood vessels, make 3D imaging the state-of-art approach for future Ca^{2+} studies addressing the role of astrocytes in brain function.

LEGENDS

Fig. 1. Gray matter astrocytes are 3D cells poorly covered by 2D imaging.

Comparative analysis of astrocyte morphology captured by 3D vs 2D two-photon imaging (*GFAP-EGFP* mice, n=21 cells). "Best 2D" focal planes (FP, z=1µm) were those containing the maximum of astrocytic fluorescence. **A)** Representative 3D stack of a EGFP-expressing astrocyte (*top, green*) and corresponding best 2D FP (*bottom, red*); **(B)** Graph showing % of astrocytic volume collected in each 2D FP relative to best FP. See also Movie S1. **(C)** Histograms show % of astrocytic (or specific region) volume contained in best 2D FP. **(D)** Maximum number of processes or end-feet and maximal process length captured by best 2D FP vs 3D. All data expressed as mean ± SEM.

Fig. 2. A 3D imaging and analysis approach to study Ca^{2+} dynamics in entire astrocytes.

Left: Entire astrocytic volumes (~30 focal planes, FP) were routinely imaged at 2Hz using a two-photon apparatus equipped with fast scan head, piezo-actuated objective, and high-sensitivity GaAsP detectors (morphology = SR101, red; Ca^{2+}= GCaMP6f, green). *Left, top*: Ca^{2+} activity (green) was analyzed voxel-by-voxel with the "structure-free method" (see Methods), producing a 3D voxel-frequency map (yellow = highly active voxels) in both structurally-resolved (core) and unresolved (gliapil) astrocytic regions. *Right, bottom*: SR101 fluorescence signal (red) was used to segment the astrocyte core (grey) and identify individual compartments (S = soma; P1, P2, P3 = Processes; EF = End-Foot). These were further sub-divided in sub-regions (see Methods). In orange, snapshot of simultaneous Ca^{2+} activity in the three processes. The bottom fly-out shows two P2 sub-regions (sized 19.4 and 8.8 µm^3, respectively) and corresponding Ca^{2+} traces. In blue highlight, time when P1, P2 and P3 were simultaneously active.

Fig. 3. 3D astrocytic Ca^{2+} activity *in vivo* and *ex vivo*: comparison with 2D.

(A) Representative 3D voxel-frequency map (and corresponding best 2D FP) of a hippocampal astrocyte in situ (VOI=57x44x21 µm^3). Color-scale: in yellow, high activity voxels. **(B)** Group data from 14 cells showing percentage of total 3D detectable activity captured by best 2D FP. See also Fig.S2 and Movie S2. **(C)** Comparison of Ca^{2+} activity

detected in cortical astrocytes from awake mice (*top row*) and in hippocampal astrocytes from acute slices (*bottom row*). *Left:* mean voxel frequency in the entire astrocyte; *right*: normalized event frequencies in each compartment. **(D)** Ca^{2+} activity distribution (in percentage) between soma, processes and end-feet (color code as in C).

Fig. 4. Astrocytic Ca^{2+} activity in processes and soma is highly heterogeneous.

 (A) *Left:* 3D reconstruction of a hippocampal astrocyte in situ (core structure): processes color-coded according to average activity level. *Right:* distribution of all processes from recordings in situ (n=72) based on individual mean Ca^{2+} activity. See also Fig. S4A,B. **(B)** Effect of TTX on basal Ca^{2+} activity in individual processes in situ (n=21); color-coding highlights different levels of inhibition (high: >75%; medium 25-75%; no: <25%). **(C)** Voxel-activity map showing microscopic heterogeneity of Ca^{2+} activity within each process and surroundings (P1, P2 = Processes, S = Soma, EF = End-Foot, g = Gliapil; voxel size =$1\mu m^3$). Notice hot spots (yellow) and cold regions (brown) along the process. **(D)** Distribution of local Ca^{2+} activity within each individual process vs distance from soma (n=17 medium/high-activity processes). Activity calculated voxel-by-voxel (size=$1\mu m^3$) and normalized to maximal activity in the process. Asterisks denote endfoot-related processes. **(E)** *Left:* Distribution of spatial spread vs total duration (semi-logarithmic scale) of Ca^{2+} events involving the astrocytic soma (*ex vivo*, n=29; *in vivo,* n=11); *Right*: representative examples of spatially heterogeneous somatic events overlaid on the astrocytic morphology (red: *ex vivo*; green: *in vivo*). See also Fig. S4C. **(F)** Temporal cross-correlation projection map (30-µm stack) of GCaMP6f activity indicating multifocal origination of a global event *in vivo*: "lead" voxels (shades of red) preceding main event cluster at the astrocyte periphery, mainly in gliapil. Core structure outlined; b.v.=blood vessel. See also Fig. S6.

Fig. 5. End-feet of the same astrocyte are independently active but occasionally show local or global coordination.

(A) Confocal 3D stack (z=33 µm) of a hippocampal astrocyte from a *GFAP-EGFP* mouse. End-feet (e.f.1, 2, 3, 4) and processes identified by GFAP staining (cyan), red blood vessel outline by AQP4 (green), nucleus by DAPI (magenta). **(B)** Representative Ca^{2+} traces showing activity in two end-feet of the same astrocyte; *Top: ex vivo* (e.f.1 and 2 refer to organization in A); *Bottom: in vivo* (e.f.1 and 3). In orange highlight, asynchronous events; in grey highlight: synchronous events, most independent of somatic (S) Ca^{2+} elevation, except one *in vivo,* part of a global event. **(C)** two-photon snapshots (VOI = 56x49x31µm) showing examples of Ca^{2+} activity in a hippocampal astrocyte either confined to an end-foot (e.f., *left*) or involving also the related process (e.f. process, *right*). Corresponding traces and distribution pie charts show the former case in orange highlight and the latter in green highlight.

Fig. 6. Hippocampal axons have complex 3D morphological interactions with astrocytes: a functional study with 3D Ca^{2+} imaging. (A) Axonal tracing experiment to study axon-astrocyte interactions. Perforant path (PP) axons (red) highlighted upon viral injection of red-fluorescent tdTomato in entorhinal cortex (EC), astrocytes upon loading with SR101 (displayed in white). (*Left*): large view of the fluorescent axonal fibers in the hippocampal formation; (*right*) higher zoom of the squared region on the left, showing arrival of PP axons in the lateral and medial dentate molecular layers and their complex intermingling with astrocytes. See also Fig. S9. **(B)** *Left*: Histograms showing mean lateral and vertical deviation of fluorescently-labelled PP axons (length followed: 108±15µm, range 32-251µm; n=20 axons). *Right*: 3D reconstruction of five axons from the same slice artificially aligned to the start point to visualize 3D deviations. In red, box representing a typical astrocytic VOI imaged in our 3D Ca^{2+} experiments; in cyan, individual 2D focal plane. The box, but not the plane, contains most of the axonal deviations, and is therefore appropriate to study axon-astrocyte functional interactions. See also Movie S4. **(C)** Targeted axonal electrical stimulation causes reliable Ca^{2+} increase detectable in a single fiber expressing the red GECI, jRCaMP1a. *Left, top*: setting for axonal stimulation experiments, showing quantum-dot-coated (QD) fluorescent tip of stimulating pipette, axonal fiber of interest (blue dotted line) and ROI (blue) along the axonal path from which

we recorded Ca^{2+} signals. *Bottom:* trace of graded Ca^{2+} increases in the ROI upon 1 to 5 brief electrical stimulations (red arrows: 50 Hz, inter-pulse interval: 20s). At the end, larger Ca^{2+} elevation induced by tetanic stimulation (red block, 100 pulses at 100 Hz). In blue: raw jRCaMP1a trace, in black: trace filtered with Gaussian filter σ=0.5s; λ=1020nm). *Right*: in a different experiment, average Ca^{2+} trace from several activated fibers showing stable response to repetitions of the above protocol at 2-3 min intervals (λ=965 nm). This response is fully blocked by TTX (1 µM).

Fig. 7. Astrocytes detect and respond to minimal axonal stimulation in a small portion of their volume. (A) Representative targeted axonal stimulation experiment. *Left*: Setting: QD stimulation pipette positioned >40 µm away from a GCaMP6f-expressing astrocyte and adjacent to tdTomato-labelled axons (blue dotted highlight) crossing the astrocytic territory. *Middle*: zoom in of squared region on the left (z-projection of 20µm stack). Magenta color-coding highlights a computationally identified "reliably responding" region, displaying Ca^{2+} elevations temporally correlated to minimal stimulation of adjacent axons (protocol as in Fig. 6C). *Right*: 15-minute trace of the astrocytic GCaMP6f signal extracted from the responding region. The zoom-in highlights astrocytic Ca^{2+} responses also to single action potential pulses (first and sixth arrows). See also Fig. S9 and Text S1 regarding spontaneous activity in non-stimulation periods. **(B)** *Left:* Effect of TTX on the region reliably responding to axonal stimulation (magenta). In green, a non-responding region of equal size, arbitrarily selected; *Middle*: GCaMP6f traces extracted from "reliably responding" region (magenta) and "non-responding" region (green) in CTRL and TTX. TTX suppresses "evoked" Ca^{2+} responses in the responding region, but does not visibly affect spontaneous activity in both regions. *Right*: TTX significantly reduces the astrocytic volume reliably responding to axonal stimulation (circles, n=6; p<0.05 Wilcoxon signed-rank test; triangles: additional n=6 CTRLs without TTX). **(C)** Representative dual GECI experiment; *Left*: Setting: QD-coated pipette adjacent to a jRCaMP1a-expressing axon (traced in cyan) approaching a GCaMP6f-expressing astrocyte. *Middle*: time-aligned axonal and astrocytic Ca^{2+} responses to minimal axonal stimuli, extracted in the VOIs on the left (axon: blue; 11.3µm³; astrocyte: orange; 2.5µm³). Raw axonal jRCaMP1a response

(cyan) overlaid with filtered trace (5 points, black). Astrocyte response is slightly delayed. TTX abolishes both axonal and astrocytic Ca^{2+} responses. *Right*: zoom-in showing timings of axonal and astrocytic responses to the middle three stimuli. Arrows denote onset of stimuli.

References:
1. K. E. Poskanzer, R. Yuste, Astrocytes regulate cortical state switching in vivo. *PNAS* **113**, E2675-2684 (2016).
2. A. Volterra, N. Liaudet, I. Savtchouk, Astrocyte Ca(2)(+) signalling: an unexpected complexity. *Nature reviews. Neuroscience* **15**, 327-335 (2014).
3. A. Araque *et al.*, Gliotransmitters travel in time and space. *Neuron* **81**, 728-739 (2014).
4. G. Perea, M. Navarrete, A. Araque, Tripartite synapses: astrocytes process and control synaptic information. *Trends Neurosci* **32**, 421-431 (2009).
5. N. Bazargani, D. Attwell, Astrocyte calcium signaling: the third wave. *Nature neuroscience* **19**, 182-189 (2016).
6. B. A. MacVicar, E. A. Newman, Astrocyte regulation of blood flow in the brain. *Cold Spring Harbor perspectives in biology* **7**, (2015).
7. J. Schummers, H. Yu, M. Sur, Tuned responses of astrocytes and their influence on hemodynamic signals in the visual cortex. *Science* **320**, 1638-1643 (2008).
8. A. Nimmerjahn, E. A. Mukamel, M. J. Schnitzer, Motor behavior activates Bergmann glial networks. *Neuron* **62**, 400-412 (2009).
9. K. Kanemaru *et al.*, In vivo visualization of subtle, transient, and local activity of astrocytes using an ultrasensitive Ca(2+) indicator. *Cell reports* **8**, 311-318 (2014).
10. X. Wang *et al.*, Astrocytic Ca2+ signaling evoked by sensory stimulation in vivo. *Nature neuroscience* **9**, 816-823 (2006).
11. M. Navarrete *et al.*, Astrocytes mediate in vivo cholinergic-induced synaptic plasticity. *PLoS Biol* **10**, e1001259 (2012).
12. C. Henneberger, T. Papouin, S. H. Oliet, D. A. Rusakov, Long-term potentiation depends on release of D-serine from astrocytes. *Nature* **463**, 232-236 (2010).
13. R. Min, T. Nevian, Astrocyte signaling controls spike timing-dependent depression at neocortical synapses. *Nature neuroscience* **15**, 746-753 (2012).
14. M. A. Di Castro *et al.*, Local Ca2+ detection and modulation of synaptic release by astrocytes. *Nature neuroscience* **14**, 1276-1284 (2011).
15. A. Panatier *et al.*, Astrocytes are endogenous regulators of basal transmission at central synapses. *Cell* **146**, 785-798 (2011).
16. G. R. Gordon, H. B. Choi, R. L. Rungta, G. C. Ellis-Davies, B. A. MacVicar, Brain metabolism dictates the polarity of astrocyte control over arterioles. *Nature* **456**, 745-749 (2008).
17. I. R. Winship, N. Plaa, T. H. Murphy, Rapid astrocyte calcium signals correlate with neuronal activity and onset of the hemodynamic response in vivo. *The Journal of neuroscience* **27**, 6268-6272 (2007).
18. H. L. Xu *et al.*, Astrocytes are a key conduit for upstream signaling of vasodilation during cerebral cortical neuronal activation in vivo. *American journal of physiology. Heart and circulatory physiology* **294**, H622-632 (2008).
19. M. R. Metea, E. A. Newman, Glial cells dilate and constrict blood vessels: a mechanism of neurovascular coupling. *The Journal of neuroscience* **26**, 2862-2870 (2006).

20. B. L. Lind, A. R. Brazhe, S. B. Jessen, F. C. Tan, M. J. Lauritzen, Rapid stimulus-evoked astrocyte Ca2+ elevations and hemodynamic responses in mouse somatosensory cortex in vivo. *PNAS* **110**, E4678-4687 (2013).

21. Y. Otsu *et al.*, Calcium dynamics in astrocyte processes during neurovascular coupling. *Nature neuroscience* **18**, 210-218 (2015).

22. C. Agulhon, T. A. Fiacco, K. D. McCarthy, Hippocampal short- and long-term plasticity are not modulated by astrocyte Ca2+ signaling. *Science* **327**, 1250-1254 (2010).

23. W. Sun *et al.*, Glutamate-dependent neuroglial calcium signaling differs between young and adult brain. *Science* **339**, 197-200 (2013).

24. K. Nizar *et al.*, In vivo stimulus-induced vasodilation occurs without IP3 receptor activation and may precede astrocytic calcium increase. *The Journal of neuroscience* **33**, 8411-8422 (2013).

25. D. E. Bonder, K. D. McCarthy, Astrocytic Gq-GPCR-linked IP3R-dependent Ca2+ signaling does not mediate neurovascular coupling in mouse visual cortex in vivo. *The Journal of neuroscience* **34**, 13139-13150 (2014).

26. M. D. Haustein *et al.*, Conditions and constraints for astrocyte calcium signaling in the hippocampal mossy fiber pathway. *Neuron* **82**, 413-429 (2014).

27. W. Gobel, B. M. Kampa, F. Helmchen, Imaging cellular network dynamics in three dimensions using fast 3D laser scanning. *Nature methods* **4**, 73-79 (2007).

28. T. W. Chen *et al.*, Ultrasensitive fluorescent proteins for imaging neuronal activity. *Nature* **499**, 295-300 (2013).

29. H. Dana *et al.*, Sensitive red protein calcium indicators for imaging neural activity. *eLife* **5**, (2016).

30. R. Srinivasan *et al.*, Ca(2+) signaling in astrocytes from Ip3r2(-/-) mice in brain slices and during startle responses in vivo. *Nature neuroscience* **18**, 708-717 (2015).

31. K. J. Sekiguchi *et al.*, Imaging large-scale cellular activity in spinal cord of freely behaving mice. *Nature communications* **7**, 11450 (2016).

32. P. O. Polack, J. Friedman, P. Golshani, Cellular mechanisms of brain state-dependent gain modulation in visual cortex. *Nature neuroscience* **16**, 1331-1339 (2013).

33. M. Avoli *et al.*, Synchronous GABA-mediated potentials and epileptiform discharges in the rat limbic system in vitro. *The Journal of neuroscience* **16**, 3912-3924 (1996).

34. M. P. Witter, The perforant path: projections from the entorhinal cortex to the dentate gyrus. *Prog Brain Res* **163**, 43-61 (2007).

35. N. V. Povysheva *et al.*, Properties of excitatory synaptic responses in fast-spiking interneurons and pyramidal cells from monkey and rat prefrontal cortex. *Cerebral cortex* **16**, 541-552 (2006).

36. M. Paukert *et al.*, Norepinephrine controls astroglial responsiveness to local circuit activity. *Neuron* **82**, 1263-1270 (2014).

37. K. Zheng *et al.*, Time-Resolved Imaging Reveals Heterogeneous Landscapes of Nanomolar Ca(2+) in Neurons and Astroglia. *Neuron* **88**, 277-288 (2015).

38. J. G. Jackson, M. B. Robinson, Reciprocal Regulation of Mitochondrial Dynamics and Calcium Signaling in Astrocyte Processes. *The Journal of neuroscience : the official journal of the Society for Neuroscience* **35**, 15199-15213 (2015).

39. A. Agarwal *et al.*, Transient Opening of the Mitochondrial Permeability Transition Pore Induces Microdomain Calcium Transients in Astrocyte Processes. *Neuron* **93**, 587-605 e587 (2017).

40. K. J. Kim *et al.*, Astrocyte contributions to flow/pressure-evoked parenchymal arteriole vasoconstriction. *The Journal of neuroscience* **35**, 8245-8257 (2015).

41. K. Schulz *et al.*, Simultaneous BOLD fMRI and fiber-optic calcium recording in rat neocortex. *Nature methods* **9**, 597-602 (2012).

42. W. J. Nett, S. H. Oloff, K. D. McCarthy, Hippocampal astrocytes in situ exhibit calcium oscillations that occur independent of neuronal activity. *Journal of neurophysiology* **87**, 528-537 (2002).

43. P. G. Hirrlinger, A. Scheller, C. Braun, J. Hirrlinger, F. Kirchhoff, Temporal control of gene recombination in astrocytes by transgenic expression of the tamoxifen-inducible DNA recombinase variant CreERT2. *Glia* **54**, 11-20 (2006).

44. C. Nolte *et al.*, GFAP promoter-controlled EGFP-expressing transgenic mice: a tool to visualize astrocytes and astrogliosis in living brain tissue. *Glia* **33**, 72-86 (2001).

45. S. Habbas *et al.*, Neuroinflammatory TNFalpha Impairs Memory via Astrocyte Signaling. *Cell* **163**, 1730-1741 (2015).

46. J. Ding, A. F. Luo, L. Hu, D. Wang, F. Shao, Structural basis of the ultrasensitive calcium indicator GCaMP6. *Science China. Life sciences* **57**, 269-274 (2014).

47. A. Nimmerjahn, F. Kirchhoff, J. N. Kerr, F. Helmchen, Sulforhodamine 101 as a specific marker of astroglia in the neocortex in vivo. *Nature methods* **1**, 31-37 (2004).

48. C. Schnell, Y. Hagos, S. Hulsmann, Active sulforhodamine 101 uptake into hippocampal astrocytes. *PloS one* **7**, e49398 (2012).

49. A. Holtmaat *et al.*, Long-term, high-resolution imaging in the mouse neocortex through a chronic cranial window. *Nature protocols* **4**, 1128-1144 (2009).

50. K. Masamoto *et al.*, Repeated longitudinal in vivo imaging of neuro-glio-vascular unit at the peripheral boundary of ischemia in mouse cerebral cortex. *Neuroscience* **212**, 190-200 (2012).

51. N. Medvedev *et al.*, Glia selectively approach synapses on thin dendritic spines. *Philosophical transactions of the Royal Society of London. Series B, Biological sciences* **369**, 20140047 (2014).

52. B. K. Andrasfalvy *et al.*, Quantum dot-based multiphoton fluorescent pipettes for targeted neuronal electrophysiology. *Nature methods* **11**, 1237-1241 (2014).

53. M. Raastad, Extracellular activation of unitary excitatory synapses between hippocampal CA3 and CA1 pyramidal cells. *The European journal of neuroscience* **7**, 1882-1888 (1995).

54. E. Meijering *et al.*, Design and validation of a tool for neurite tracing and analysis in fluorescence microscopy images. *Cytometry. Part A : the journal of the International Society for Analytical Cytology* **58**, 167-176 (2004).

55. H. R. Parri, T. M. Gould, V. Crunelli, Spontaneous astrocytic Ca2+ oscillations in situ drive NMDAR-mediated neuronal excitation. *Nature neuroscience* **4**, 803-812 (2001).

56.   F. Aguado, J. F. Espinosa-Parrilla, M. A. Carmona, E. Soriano, Neuronal activity regulates correlated network properties of spontaneous calcium transients in astrocytes in situ. *The Journal of neuroscience* **22**, 9430-9444 (2002).
57.   E. Barat *et al.*, Subthalamic nucleus electrical stimulation modulates calcium activity of nigral astrocytes. *PloS one* **7**, e41793 (2012).
58.   I. Savtchouk, S. J. Liu, Remodeling of synaptic AMPA receptor subtype alters the probability and pattern of action potential firing. *The Journal of neuroscience* **31**, 501-511 (2011).
59.   I. Savtchouk *et al.*, Topological Regulation of Synaptic AMPA Receptor Expression by the RNA-Binding Protein CPEB3. *Cell reports* **17**, 86-103 (2016).
60.   P. Jourdain *et al.*, Glutamate exocytosis from astrocytes controls synaptic strength. *Nature neuroscience* **10**, 331-339 (2007).

Methods summary

We recorded Ca^{2+} signals from the entire 3D structure of an astrocyte with a fast-scanning two-photon microscope equipped with AOD or resonant scanner and piezoelectric objective z-actuator (routine rate: 60 focal planes/sec; 2 Hz). In some experiments, we recorded from 3D sub-domains (a process, and end-foot) at faster rate (10 Hz). We used a dual-indicator approach to capture both morphology (SR101, red) and Ca^{2+} (GCaMP6f, green) signals of astrocytes *in vivo*, in the somatosensory cortex of adult awake mice, and *ex vivo*, in acute hippocampal and cortical slices. In some experiments we collected astrocytic (GCaMP6f, green) and axonal (jRCaMP1a or tdTomato, red) signals simultaneously. To obtain conditional astrocyte-selective GCaMP6f expression, we crossed Rosa26-lsl-GCaMP6f mice with GFAP-CreERT2 mice. We analyzed the large datasets generated from our 3D imaging experiments with custom-written programs and two different analytical strategies. With the first one, we extracted Ca^{2+} events within the optically resolved astrocyte "core" and defined their properties. The segmented core was subdivided in macro-regions (soma, processes, end-feet) and these further split in sub-regions. Signals, detected sub-region by sub-region, were reconstructed as events by grouping adjacent simultaneously active sub-regions. With the second strategy, we extended study of Ca^{2+} dynamics to the astrocytic regions with structures below optical resolution (the "gliapil"). Analysis in this case was conducted structure-free, voxel by voxel. With the same approach, we analyzed astrocytic responses to minimal axonal stimulations in slices and astrocyte-wide Ca^{2+} elevations in awake mice. We used cross-correlation analysis to identify the small astrocytic regions responding to axonal

stimulation or the early responding regions during astrocyte-wide events. For studying 3D astrocyte morphology and its relations with blood vessels, we utilized GFAP-EGFP mice. The full list of reagents and all details are in Supplemental Methods.

Author contributions: Erika Bindocci performed all the Ca^{2+} imaging experiments in astrocytes in brain slices and part of the experiments in awake mice, the related analyses and participated to analysis development and writing of the manuscript; Iaroslav Savtchouk developed and performed the experiments on axon-astrocyte interactions and related data analysis, supervised some of the experiments in brain slices and participated to experiments in vivo in awake mice, developed analytical tools, participated to the development of the

main analysis methods and contributed to the writing of the paper; Nicolas Liaudet developed the main original analytical methods used in the study, created user-friendly software for the other authors, interacted with companies and other authors to define the appropriate microscopy tools and conditions for 3D dynamic imaging, performed data analysis and participated to writing of the manuscript; Denise Becker developed and performed Ca^{2+} imaging in awake mice, performed immunohistochemistry and data analysis, and participated in the writing of the manuscript; Giovanni Carriero, performed all the viral injections and two photon acquisitions for morphometric analyses and participated to the in vivo experiments in awake mice; Andrea Volterra conceived and supervised the project and wrote the manuscript together with the other authors.

Supplementary Materials:

Materials and Methods

Supplementary Text

Figs. S1 to S11

Table S1

Movies S1-S4

RESEARCH ARTICLE SUMMARY

INTRODUCTION

Astrocytes translate incoming information and generate functional outputs via Ca^{2+} signaling. Thereby, they respond to neuronal activity, producing downstream modulation of synaptic functions, and may participate in hemodynamics regulation. Deciphering the "Ca^{2+} language" of astrocytes is therefore essential for defining their roles in brain physiology and pathology. However, the specifics of astrocytic Ca^{2+} signaling are still poorly understood, and recent studies producing inconsistent/contradictory results have fostered debate on the actual role of astrocytes in synaptic and vascular functions.

RATIONALE

A neglected potential source of inconsistencies lays in the way astrocytic Ca^{2+} signaling was studied so far, mostly by conventional 2D imaging, which assumes that sampling a single (~1 µm) focal plane is representative of the entire astrocytic cell. This is, however, dubious given that astrocytes are highly 3D cells, entertain heterogeneous 3D relations with neighboring structures, and show Ca^{2+} signals on local scale. Therefore, we developed a new method to scan three-dimensionally entire astrocytes and observe full-cell Ca^{2+} dynamics.

RESULTS

With our 3D approach we sampled astrocytes at sufficient rate to detect events >1.5 seconds throughout the cell and faster ones in selected substructures (Fig. 0). We found that Ca^{2+} activity in an individual astrocyte is heterogeneously scattered throughout the cell, largely compartmented within each region, and preponderantly local. The majority resides in the "gliapil", the peripheral region composed of fine (optically sub-resolved) structures occupying ~75% of the astrocyte volume. Within the central (resolvable) "core", soma is mostly inactive, whereas processes are frequently active, yet showing widely different activity between them. Even in individual processes, activity distributes heterogeneously, with alternating "hot" and "cold" spots.

3D imaging was performed both in adult brain slices and *in vivo*, in awake mice. Activity *in vivo* was faster and more frequent, particularly in end-feet, yet similar in properties and cellular distribution to slices, except for the presence of cell-wide "global" Ca^{2+} events mainly associated to mouse movement. Contrary to current beliefs, "global" events were not sweeping waves, but rather multifocal Ca^{2+} elevations that started at multiple gliapil loci and then spread to the core.

At the vascular interface, astrocytic Ca2+ activity was mostly restricted to individual end-feet, even to their fractions, and only occasionally coordinated with the end-foot process or the rest of the astrocyte. Two or more end-feet were mainly asynchronous, even when enwrapping the same vessel. Astrocytic structures and axons intersected three-dimensionally, and minimal axonal activity (individual action potentials), produced time-correlated astrocytic Ca^{2+} elevations in small spots (<1% of the volume), demonstrating that astrocytes can sense even the lowest levels of neuronal activity.
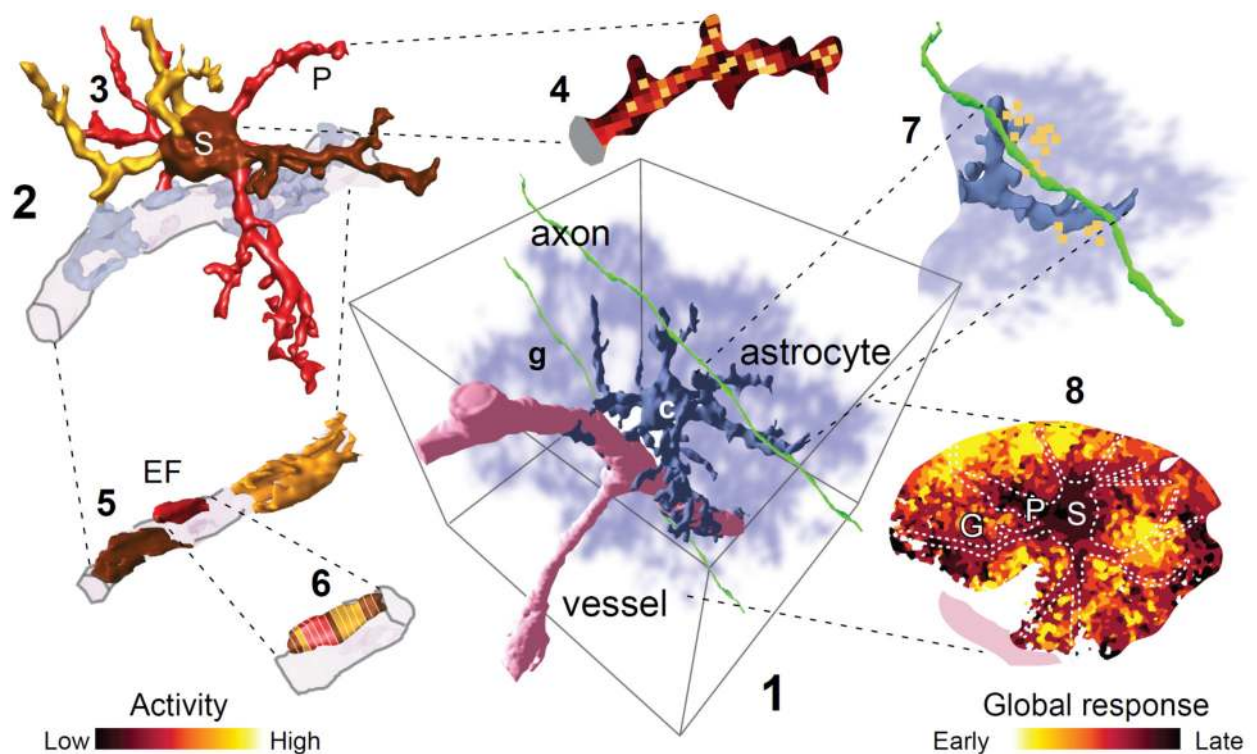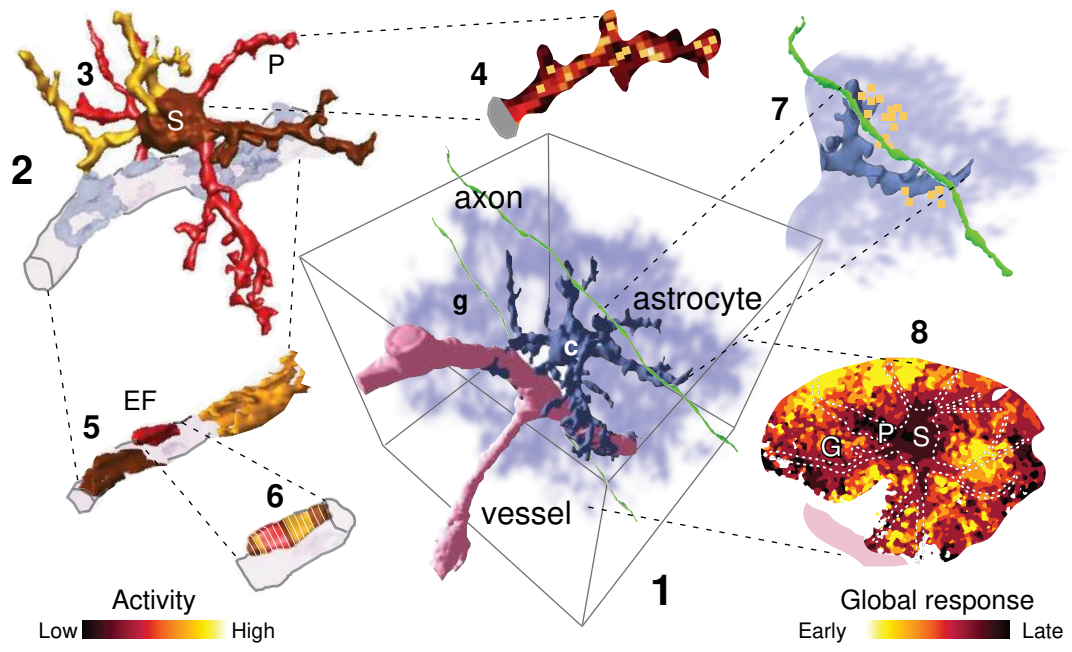
CONCLUSIONS

We provide the first comprehensive 3D map of Ca^{2+} activity in an individual astrocyte. Its widespread, heterogeneous, local and mostly three-dimensional nature confirms the appropriateness of our whole-cell imaging approach. Past 2D studies, often focusing on somatic Ca^{2+} dynamics, inadequately described the emerging richness and complexity of the astrocyte
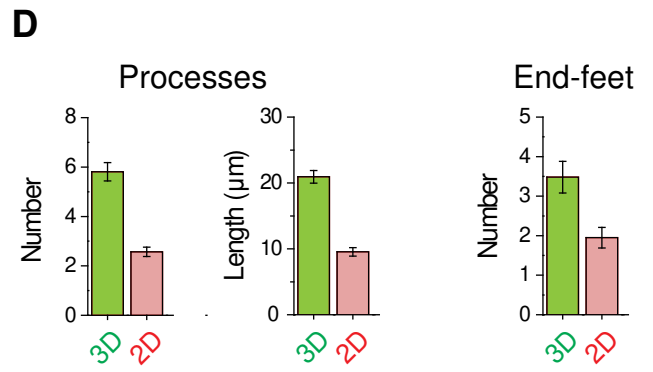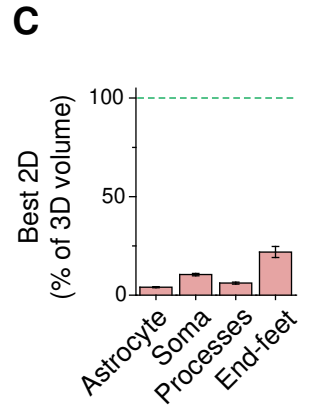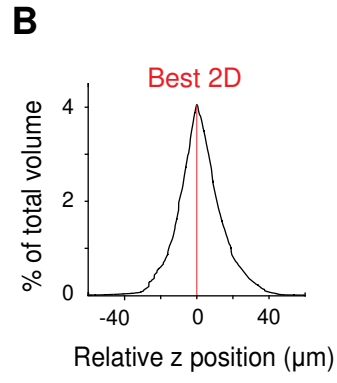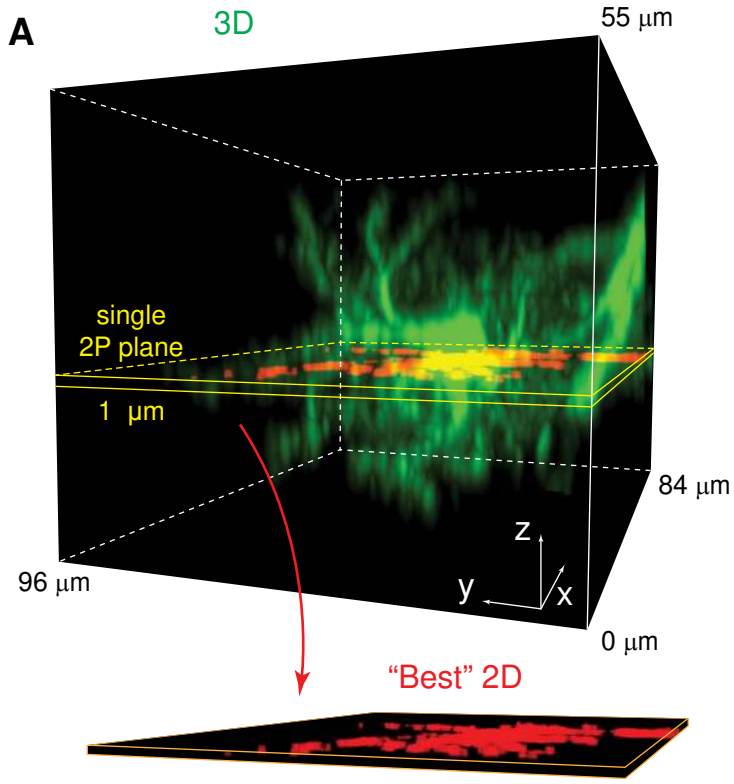
activity, notably at astrocyte-synapse and astrocyte-vascular interfaces, where activity is small, fast, and frequent. In this context, we can foresee future challenges in extending studies to the gliapil, whose structures fall below current optical resolution, and in reporting the complete gamut of astrocyte Ca^{2+} signals at the full cell scale, both requiring technical advances. Nonetheless, the here demonstrated feasibility promises to make 3D Ca^{2+} imaging the state-of-art approach for Ca^{2+} studies addressing the role of astrocytes in brain function.
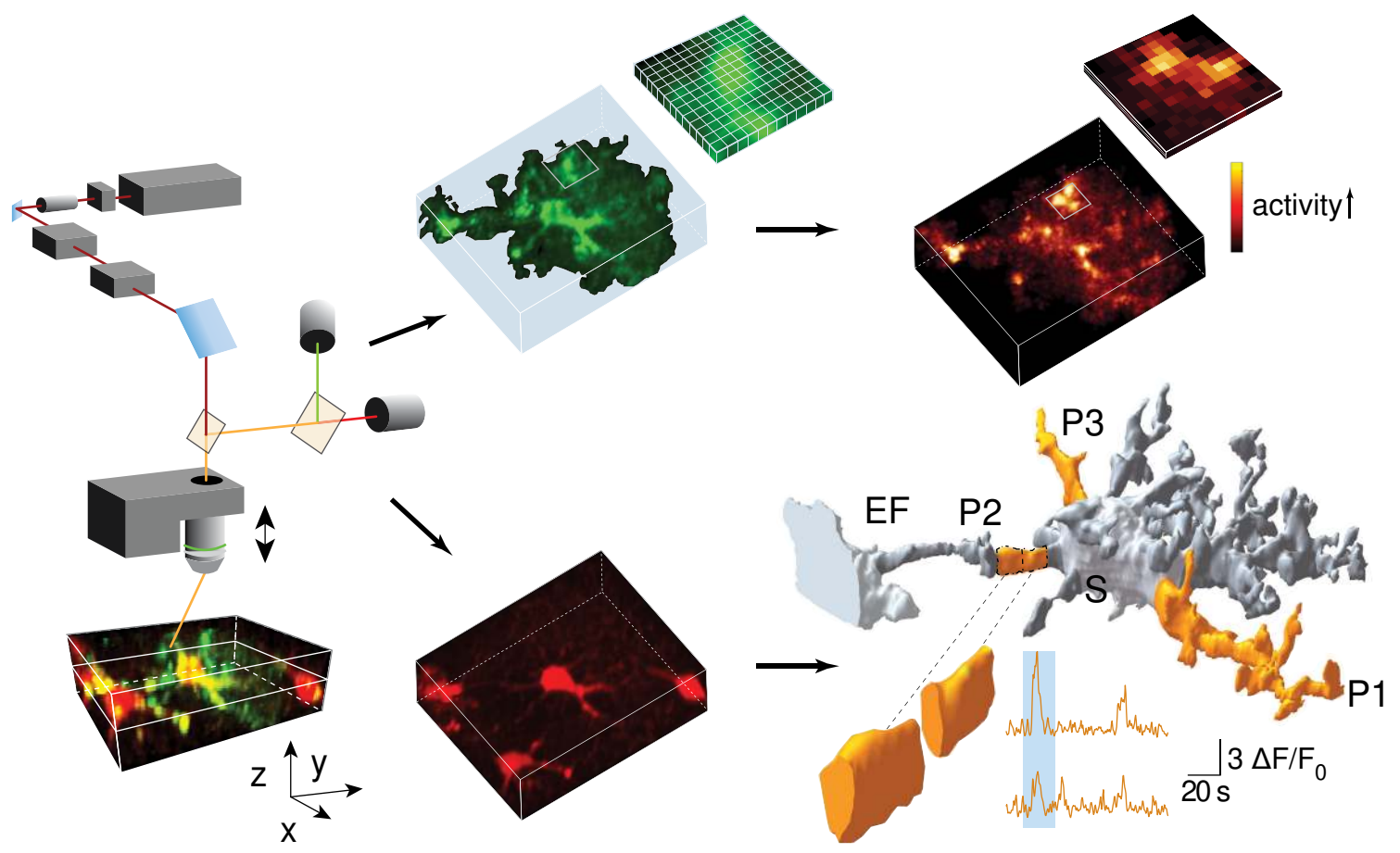
Fig. 0. 3D Ca^{2+} imaging reveals the complex activity of astrocytes
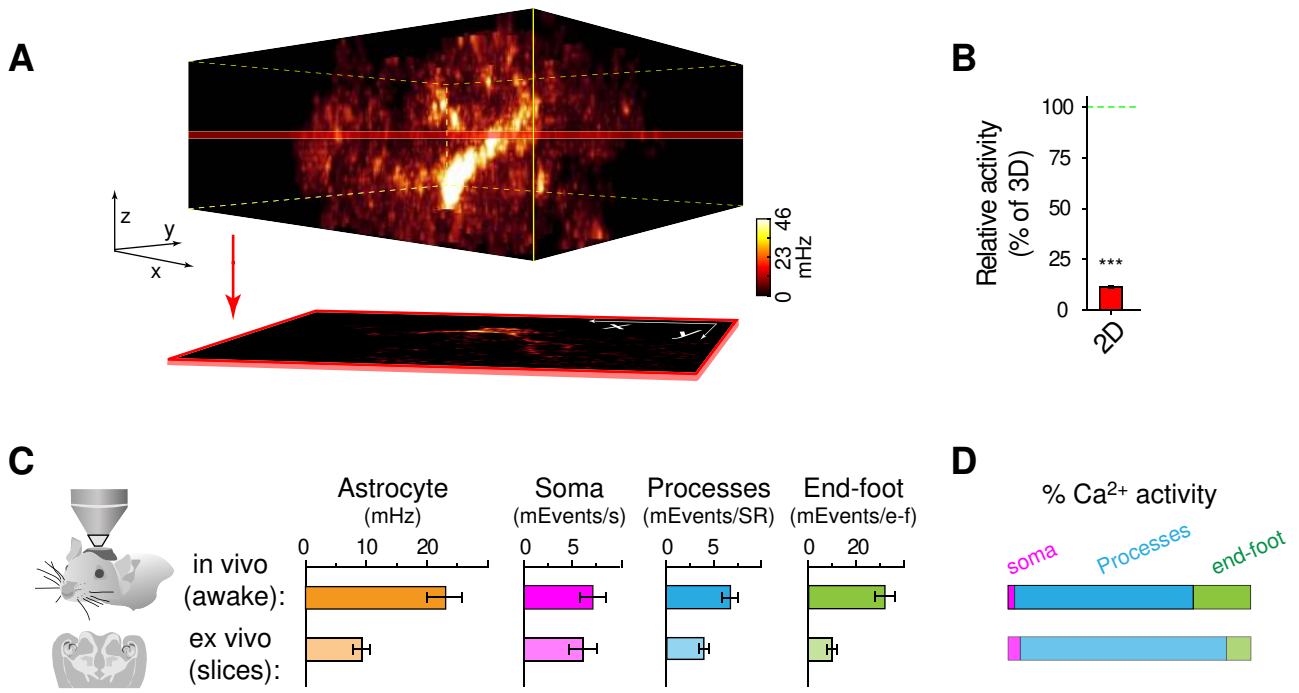
(1): Representation of the 3D structural interactions between astrocyte, axons and blood vessels. Astrocyte contains optically resolved (core, c) and unresolved (gliapil, g) regions. (2) 3D Ca^{2+}imaging reveals different activity (intensity color-scale) in different astrocytic regions (processes, P; soma, S, end-foot, EF); (3) in different processes; and (4) in different loci of individual processes. (5) It also reveals asynchronous activity in end-feet, (6) often restricted to end-foot sub-domains; and (7) local astrocyte responses to minimal axonal firing, or (8) global responses to in vivo locomotion (time color-scale).
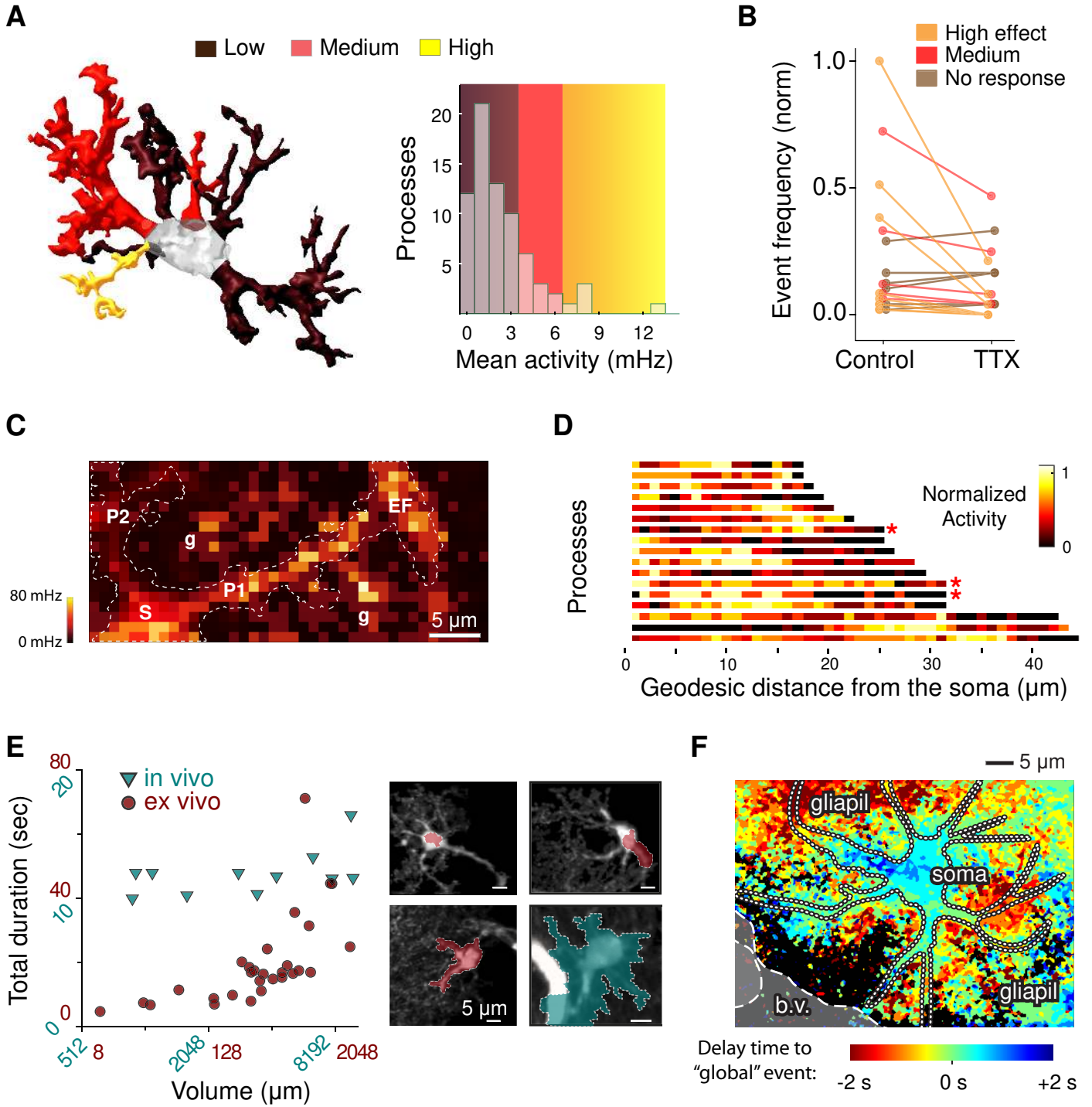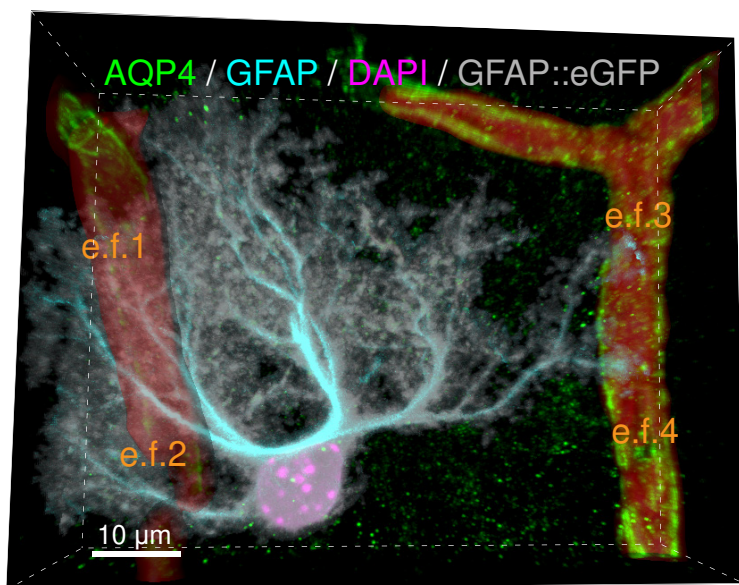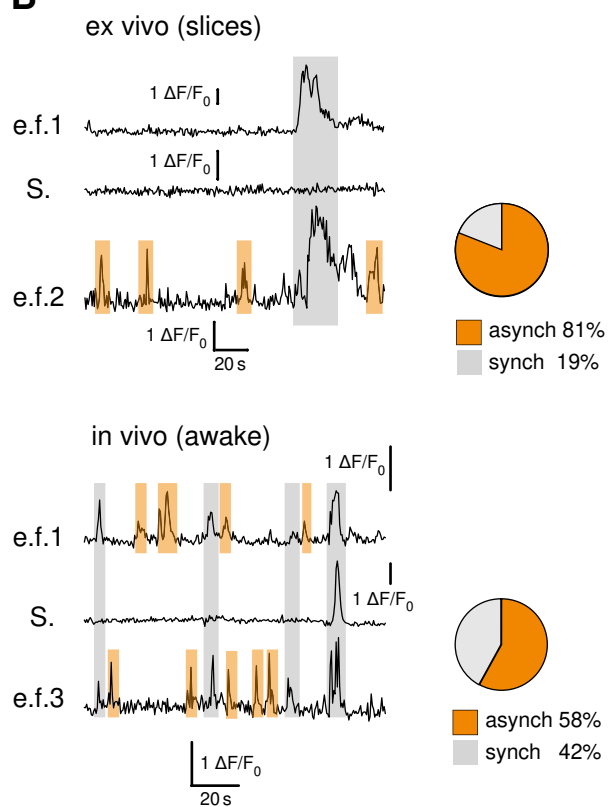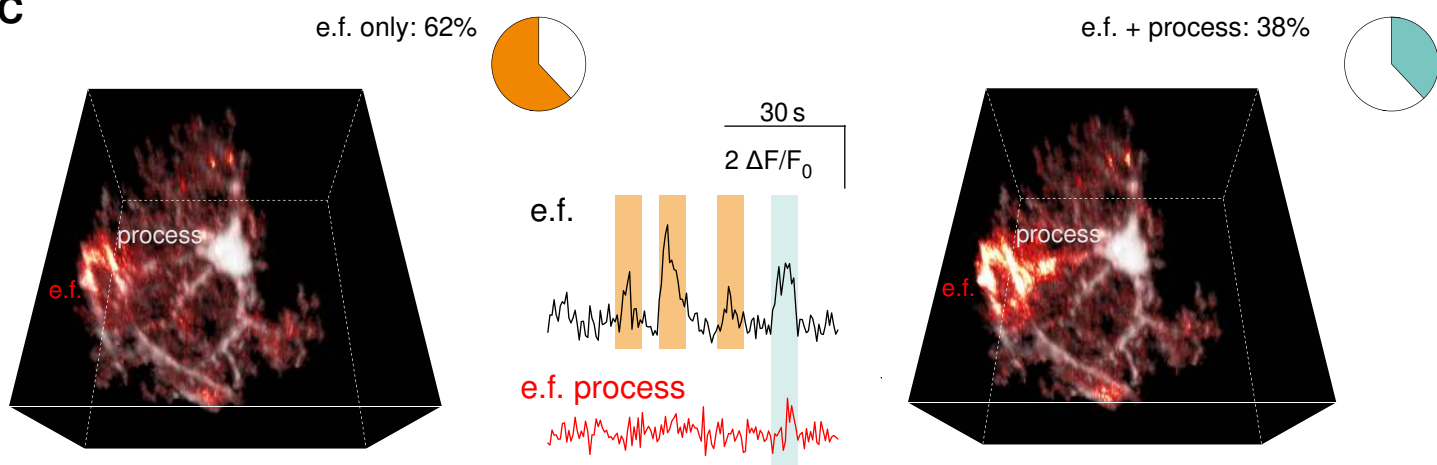
axon

astrocyte

vessel

g

c

P

S

EF

Activity

Low High

Global response

Early Late

G P S

1 2 3 4 5 6 7 8

A

3D

55 μm

single
2P plane

1 μm

96 μm

84 μm

z

y x

0 μm

"Best" 2D

B

Best 2D

% of total volume

4

2

0

-40   0   40

Relative z position (μm)

C

Best 2D
(% of 3D volume)

100

50

0

Astrocyte Soma Processes End-feet

D

Processes

Number

8

6

4

2

0

3D   2D

Length (μm)

30

20

10

0

3D   2D

End-feet

Number

5

4

3

2

1

0

3D   2D

activity↑

P3

EF   P2

S

P1

3 ΔF/F₀
20 s

z y
   x

A

B

C

D

A

Low | Medium | High

B
High effect
Medium
No response

Event frequency (norm)

Control | TTX

Mean activity (mHz)
Processes

C

80 mHz
0 mHz

P2
g
EF
P1
S
g

5 µm

D

Normalized Activity

1
0

Processes

Geodesic distance from the soma (µm)

E

Total duration (sec)

in vivo
ex vivo

Volume (µm)

5 µm

F

5 µm

gliapil
soma
b.v.
gliapil

Delay time to "global" event:
-2 s | 0 s | +2 s

A

AQP4 / GFAP / DAPI / GFAP::eGFP

e.f.1

e.f.2

e.f.3

e.f.4

10 μm

B

ex vivo (slices)

1 ΔF/F$_0$

e.f.1

1 ΔF/F$_0$

S.

e.f.2

1 ΔF/F$_0$ 20 s

asynch 81%
synch 19%

in vivo (awake)

1 ΔF/F$_0$

e.f.1

S.   1 ΔF/F$_0$

e.f.3

1 ΔF/F$_0$
20 s

asynch 58%
synch 42%

C

e.f. only: 62%

process

e.f.

30 s

2 ΔF/F$_0$

e.f.

e.f. process

e.f. + process: 38%

process

e.f.

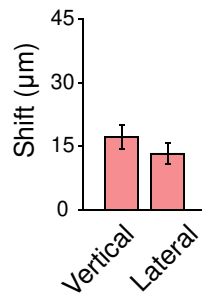**A**

λ_{2p}= 920 / 1020
SR101 / tdTom

Viral injection site (EC)

500 μm

40 μm

B

Axonal displacement per 50 μm of length

Shift (μm)

Vertical Lateral

60 μm

225 μm

70 μm

0 μm

C

λ_{2p}= 1020 jRCaMP1a / QD-Pip

10 μm
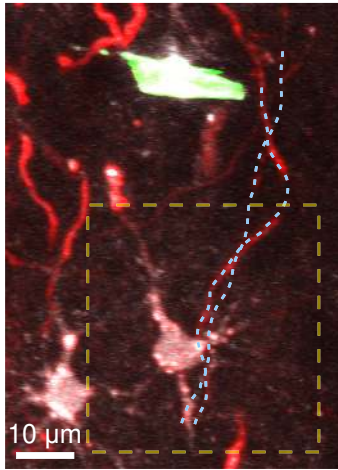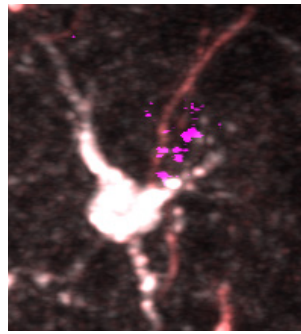
20 au 30 s

— raw
— filtered

CTRL

TTX

2 min
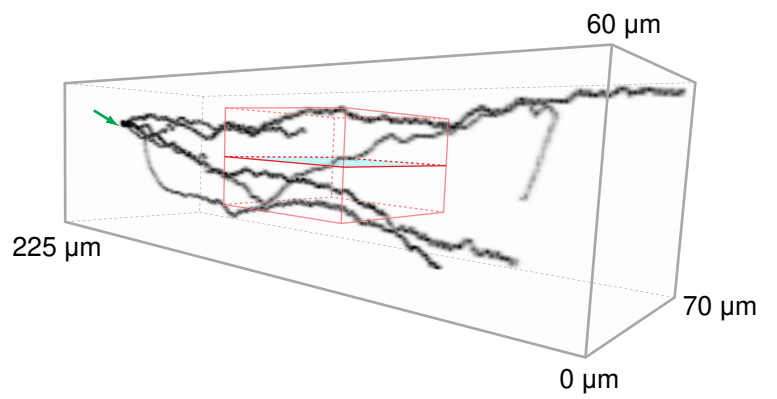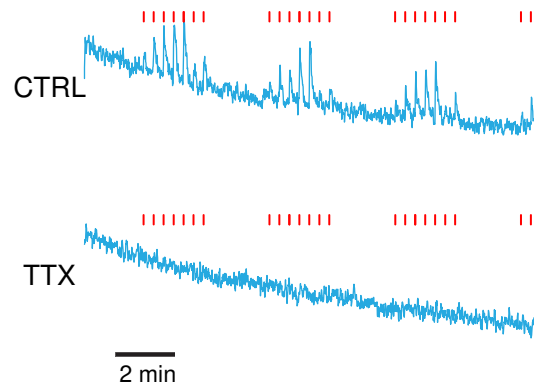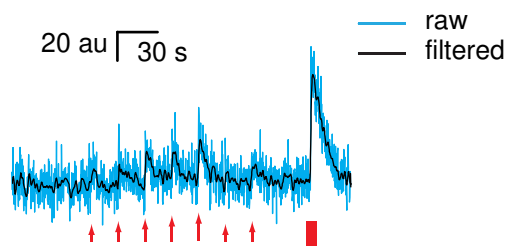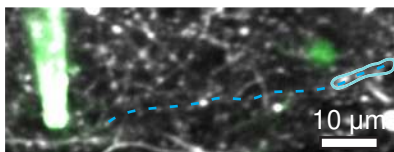
A

SR101/tdTomato/QD-Pipette

Astrocyte / Axons / Responding

GCaMP6f (Responding)

10 µm

2 min

B
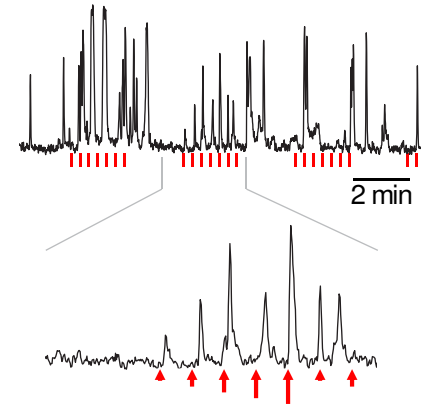
GCaMP6f / Responding / non-responding

CTRL   TTX

10 µm

Reliably-responding regns

CTRL   TTX

20 au

2 min

A non-responding region

CTRL   TTX
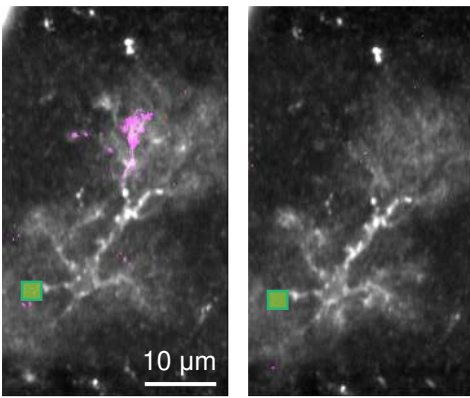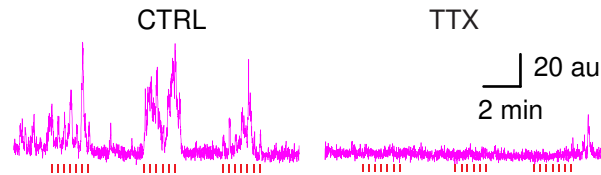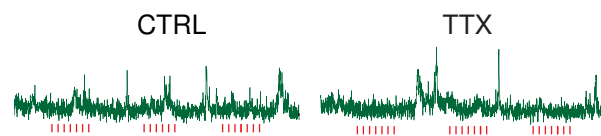
Responding volume (% of total)

CTRL   TTX
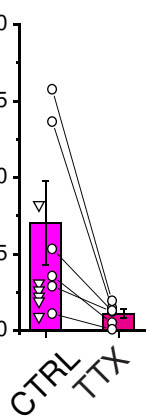
C

Axonal Ca²⁺
Astrocytic Ca²⁺
Running average

SR101 / QD-Pip / target axon

15 µm

0.2 ΔF/F₀

20 s   2 ΔF/F₀

0.2 ΔF/F₀

2 ΔF/F₀

+TTX

0.2 ΔF/F₀

2 ΔF/F₀

20 s
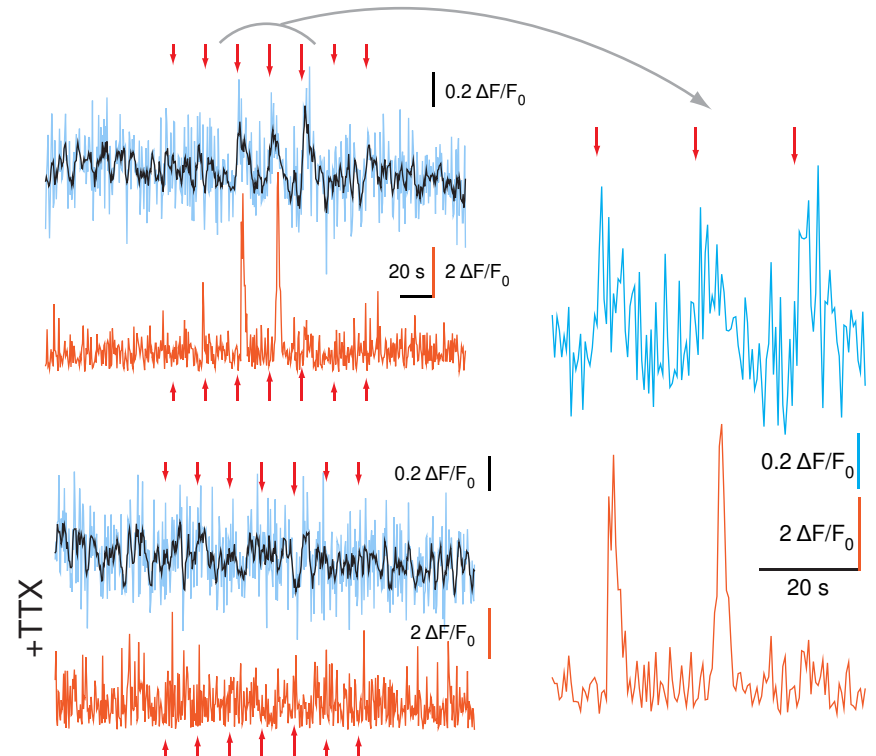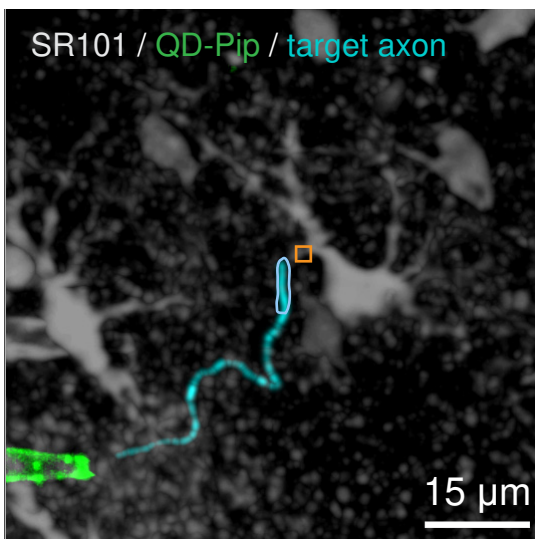
Supplementary Materials for

3D Ca^{2+} Imaging Advances Understanding Of Astrocyte Biology

Erika Bindocci†, Iaroslav Savtchouk†, Nicolas Liaudet†, Denise Becker, Giovanni Carriero and
Andrea Volterra*
correspondence to: andrea.volterra@unil.ch
†, co-first author, equal contribution

This PDF file includes:

Other Supplementary Materials for this manuscript includes the following:

Materials and Methods

<u>Antibodies and chemicals</u>

Antibodies and chemicals Primary antibody polyclonal GFP (chicken) was from Aves Labs Inc., Oregon, USA (GFP-1010); polyclonal glutamine synthetase (rabbit) from Abcam, Cambridge, UK (ab73593); monoclonal NeuN (mouse) from Merck SA, Switzerland (MAB377); aquaporin-4 (rabbit, ab2218) and monoclonal glial fibrillary acidic protein (GFAP) antibody (mouse, ab3402) were from Millipore. Secondary antibodies Alexa Fluor 555 (rabbit), Alexa Fluor 488 (chicken and mouse) and Alexa Fluor 633 (chicken and mouse) as well as 4′,6-diamidino-2-phenylindole (DAPI) were from Thermo Fisher Scientific Inc., MA USA. 4-aminopyridine (4-AP) was from Tocris Bioscience, Bristol, UK (ref.0940); Tetrodotoxin (TTX) from Latoxan, France (ref L8503). All the other chemicals were from Sigma-Aldrich.

<u>Transgenic mice</u>

For astrocyte Ca^{2+} imaging experiments, two transgenic mouse lines, a *lox-STOP- lox-cytosolicGCaMP6f* (purchased from The Jackson Laboratory http://www.jax.org, JAX 024105 (*B6;-Gt(ROSA)26Sortm95.1(CAG-GCaMP6f)Hze/J*), and *hGFAPCreERT2* (*43*) obtained from Prof. F. Kirchhoff, University of Saarland, Germany, were crossed in order to get inducible, astrocyte-specific, cytosolic GCaMP6f expression (*GFAPCreERT2xGCAMP6f* mice). At P21, double transgenic animals of both genders were weaned and group-housed. At a given age, which depended on the type of experiment (see below), mice were then treated with Tamoxifen, to induce Cre-loxP recombination via nuclear translocation of Cre-ERT2 and trigger GCaMP6f expression. Tamoxifen was dissolved in corn oil (10mg/ml) and administered i.p. (0.1 ml/10 g body weight) over 2-3 days. Ca^{2+} imaging experiments in hippocampal slices were performed 10-14 days after the first Tamoxifen injection, when GCaMP6f expression was astrocyte-specific in the whole hippocampus, except for a small sub-population of neural stem cells/immature neurons in the dentate gyrus (for details see Fig. S1). For most of these experiments mice were used at P30-P65. Experiments in cortical slices were performed in older mice (4 months) to allow comparison with the in vivo dataset (see below); in this area of the brain GCaMP6f expression was astrocyte-specific even several weeks after Tamoxifen injections. In experiments involving axonal stimulation, mice were 2-4 months-old because of preceding AAV tracer injection procedure (see below). For *in vivo* Ca^{2+} imaging experiments, Tamoxifen was injected directly after surgery (1 time and, in some cases, 1 day later again) into 2-3 months-old mice and mice were imaged from 11 days up to 8 weeks after the first injection. For morphological analysis of astrocytes, *GFAP-EGFP* mice *(44)* were used at P30-P56.

All *in vivo* and *ex vivo* procedures on the mice here described were conducted under license and according to regulations of the Cantonal Veterinary Offices of Vaud (Switzerland).

<u>Viral constructs and injections</u>

Adeno-associated virus expressing the red fluorescent protein, tdTomato under the control of the neuronal-specific promoter, synapsin (AVV2-Syn-pQC membrane tdTomato IX, viral titer: ~$1x10^{12}$ VG/ml; provided by Tebu-Bio GmbH, Germany) was injected in layers II-III of the entorhinal cortex (mEC) of *CL7BL6* or *GFAPCreERT2xGCaMP6f* mice in order to label their axonal projections to the molecular layer of the hippocampal dentate gyrus (DG), the perforant

path (PP). In some experiments, injections in the same location were performed with an AAV expressing the red Ca^{2+} -sensitive indicator, jRCaMP1a under synapsin promoter (AAV1-Syn-NES- jRCaMP1, generously provided by L. Looger, Penn Core). To evaluate neuronal response to axonal stimulation, several mice carrying the floxed GCaMP6f gene were injected with a neuronally-targeted AAV5.CamKII:Cre virus into the Dentage Gyrus, leading to neuronal expression of the Ca^{2+} indicator. Viral injections were performed under general anesthesia using continuous isoflurane (induction: 4%; maintenance: 1-2%). After inducing anesthesia, mice were injected s.c. with Carprofen (5 mg/kg), subjected to a small craniotomy and unilaterally injected with the virus by use of a stereotaxic apparatus into the left mEC (bregma: -4.5 mm; lateral: 2.85 mm; ventral: -3.30 mm). Virus injections were performed over a period of 5 to 10 min (0.5-1 µl). At the end, the needle was left in place for 10 more minutes and then gently withdrawn. Surgical wounds were sutured and mice allowed to recover on a heating pad. To minimize pain, xylocaine gel was applied on the suture and paracetamol (500 mg/250 ml) dissolved in the drinking water of the mice. Injections were performed on P30-40 mice, then allowing at least 3-4 weeks before preparing acute slices from the transfected brains, to give cells enough time to express the fluorescent protein. Tamoxifen (needed to trigger astrocyte GCaMP6f expression) was administered 10-14 days before sacrificing the animals (see above).

Immunohistochemistry

Immunostainings were performed as previously described (*45*). Briefly, *GFAPCreERT2xGCaMP6f* mice (P39, injected with Tamoxifen at P24, see above) were sacrificed with pentobarbital and transcardially perfused first with 0.9% NaCl solution and finally with 4% (w/v) paraformaldehyde in phosphate buffer (0.1 M PB, pH 7.4). Brains were then removed and stored in phosphate buffered saline (PBS, pH 7.4). 50 µm- thick horizontal slices (respectively 70 µm for aquaporin-4, AQP4, labeling) were cut on a vibratome in PBS (pH 7.4) and stored at -20° C in a solution containing ethylene glycol (30%) and glycerol (30%) in 0.05 M PB (pH 7.4) until further processing. For immunohistochemistry, slices were rinsed in PBS (3 x 10 min) and incubated for 1 h (2 h for AQP-4 staining) in 0.5% Triton-X 100 and 10% normal horse serum (NHS) in PBS to permeabilize membranes and reduce unspecific staining. Subsequently, slices were incubated with primary antibodies (anti-GFP, chicken, 1:500; anti-NeuN, mouse, 1:1000; anti-glutamine-synthetase, rabbit; anti-AQP4, rabbit; anti-GFAP, mouse, 1:1000) in 0.1% Triton-X 100 and 5 % NHS in PBS on a horizontal shaker (24 hours, 4° C). The GFP antibody was used to reveal location of GCaMP6f protein, which contains a permutated eGFP (*46*). Then, slices were washed in PBS (3x, 10 min) and incubated with secondary antibodies (goat anti-chicken Alexa 488 or 633, goat anti-rabbit Alexa 555, goat anti-mouse Alexa 633 or 488; all 1:500) overnight at 4° C in the same solution as for primary antibodies. After further rinsing (10 min) in PBS (including 1:5000 DAPI for nuclear staining) and then (2x 15 min) in PBS, slices were mounted with Fluoromount™ Aqueous Mounting Medium.

Confocal imaging

GCaMP6f expression was visualized using a Zeiss LSM 710 confocal microscope. Laser excitation wavelength was set at: 405 nm with a diode for DAPI; 488 nm and 514 nm with an Argon laser for Alexa Fluor 488 or GFP, respectively, and Alexa Fluor 555; 633 nm with a He/Ne laser for Alexa Fluor 633. Images of whole brain sections were acquired with a 10x (0.30 NA)

objective (frame average: 4, pinhole size: 1 Airy unit, resolution 1024x1024, 7x9 single images were combined to show the whole brain section). Higher zoom z-stacks were acquired with a 40x (1.30 NA) or 63x (1.2 NA) oil immersion objectives using a software and stored as .lsm files (20-40 µm, step size: 0.5-1 µm, frame average: 4, pinhole size: 1 Airy unit, resolution 1024x1024 or 512x512). To assess cell specificity of GCaMP6f expression a z-stack acquired from the three hippocampal regions, CA1, CA3, DG, was inspected in ImageJ software. Each GFP/GCaMP6f positive cell that had a clearly identified soma (DAPI staining) was checked for double-labeling with NeuN (neuronal marker) and GS (astrocyte marker) staining.

Acute brain slice preparation

For *ex vivo* Ca^{2+} imaging experiments in brain slices, mice where anesthetized with isoflurane and decapitated. The brain was removed and quickly placed in ice-cold slicing solution containing (in mM): 105 sucrose, 62.5 NaCl, 2 KCl, 1.2 NaH2PO4, 25 NaHCO3, 0.5 CaCl2 and 7 MgCl2; pH was equilibrated with 5%/95% CO2/O2 gas mix. Horizontal, hemibrain slices (350 µm-thick) were cut, placed immediately in regular aCSF solution, containing (in mM) 118 NaCl, 2KCl, 2 MgCl2, 2 CaCl2, 25 NaHCO3, 1.2 NaH2PO4 and 10 glucose and used for the next 4-5 h at nearly physiological temperature (34 ˚C). In order to preclude development of epileptiform activity in slices, aCSF contained elevated Mg^{2+} concentration (2 mM) and no GABA inhibitors were applied in these experiments. To visualize astrocytes during imaging experiments, we loaded hippocampal or cortical slices acutely with sulforhodamine 101 (SR101), a red dye which, under the used conditions, loads specifically astrocytes in the forebrain areas studied (*47, 48*). Dye loading was performed by placing slices in a dark chamber containing SR101 (500 nM) for 15 min, at 36 ˚C. To attenuate background signal, slices were rinsed for 15 min in aCSF before the experiments. For axonal visualization experiments, slices were loaded with SR101 at a lower concentration (50 nM) for 5 min at 34 °C.

In vivo awake mouse preparation

Adult *GFAPCreERT2xGCaMP6f* mice were anesthetized with isoflurane (4% during induction; 1.5-2% for maintenance in O2) and placed on a stereotaxic frame for implantation of cranial windows as previously described (*49*). Mice were injected s.c. with carprofen (5mg/kg) to reduce pain. Body temperature was maintained at 37 °C with a heating pad, eyes covered with Viscotears and skin over the skull thoroughly disinfected. An incision in the midline of the skull was done, the skull was cleaned and dried and then a circular craniotomy (diameter: 3 mm) was drilled with a high-speed drill with the center over the somatosensory cortex, approximately -1.5 anterior-posterior (AP), 2 medio-lateral (ML) mm from bregma, right hemisphere, and the bone, but not the dura, was removed. After absorbing any bleeding with absorbent sponge and rinsing the craniotomy with sterile aCSF (125 mM NaCl, 5 mM KCl, 10 mM glucose, 10 mM HEPES, 2 mM CaCl2 and 2 mM MgSO4, pH 7.4) a round coverslip (thickness #1, 3 mm diameter) was fitted into the craniotomy, sealed with Kwik-Sil and secured with bone cement mixed with cyanoacrylate glue. Then the whole skull was covered with cyanoacrylate glue and a custom-made head bar fixed over the left hemisphere with bone cement. Around the cranial window, a little pool was formed with the cement to retain water for the imaging. After surgery, mice were allowed to recover on a heating pad and paracetamol was dissolved in their drinking water for 3 days (250mg/250ml). 4-5 days after recovery, mice started to be trained to sit head fixed under the microscope for

consecutively longer time periods. Ca^{2+} imaging was performed 2-4 weeks after cranial window implantation. 1-2 hours before imaging mice were injected i.v. or i.p. with SR 101 (5-10mg/ml in 0.9% (w/v) sterile NaCl solution, 20 mg/kg) as reported previously (*50*). In some control experiments, we omitted SR101 and did not notice obvious differences in the recorded astrocytic Ca^{2+} activity.

Two-photon 3D Ca^{2+} imaging

3D Ca^{2+} imaging experiments were performed using either of two imaging setups: setup 1 was a Bruker *in vivo* Ultima IV system equipped with a 8kHz resonant galvanometer scanner and a piezoelectric actuator, coupled to a MaiTai eHP DS laser with 70fs pulse duration, tuned to 920 nm (SR101 and GCaMP6f in astrocytes) or 1020 nm (tdTomato or jRCaMP1a in axons). For dual Ca^{2+} indicator experiments (simultaneous jRCaMP1a/GCaMP6f), the wavelength was set to 965 nm. Negative dispersion was optimized for each wavelength. Laser power was rapidly modulated by a Pockels cell. Imaging in brain slices and *in vivo* was performed with a 20x LUMPFL60X W/IR-2 NA 0.9 Olympus objective objective. Green (GCaMP6f) and red (SR101) fluorescences were separated by a dichroic beam splitter (t560lpxr) and passed through, respectively, an et520/40m-2p and an et610/75m-2p emission filter before being collected by GaAsP detectors. Setup 2 comprised a Bruker Ultima system equipped with an AOD scanner and a piezoelectric actuator. The light source was a Chameleon Vision II Ti:Sa laser, with 140fs pulse duration, tuned to 920 nm and negative dispersion was optimized to the used wavelength. The laser power was rapidly modulated by a Pockels cell. The set of dichroics and filters used was identical to that in setup 1, and green and red florescence were respectively collected by a GaAsP and a multi-alkali PMT. Combination of an AOD or resonant scanner with a piezoelectric actuator allows for high-speed 3D imaging (see below), while highly sensitive GaAsP detectors with negative dispersion allow for minimal laser dose applied to biological samples, a critical feature for relatively long-term acquisitions with no photo-damage. The laser power was varied based on the depth of the cell and imaging conditions, but in general, we used 3-4 mW for slices, and between 9-20 mW *in vivo*, depending on depth and cranial window condition, measured exiting the objective.

Experiments in brain slices were performed at 34˚C under constant aCSF flow. In hippocampal experiments, astrocytes were imaged in the CA1 (stratum radiatum) and DG (medial and outer molecular layers) regions. Cells with soma positioned 30-50 μm below the slice surface were selected for imaging based on their healthy appearance (revealed by SR101), isolation from other GCaMP6f-expressing astrocytes and low basal calcium signal (revealed by GCaMP6f). In whole cell experiments, to image the entire astrocyte over time, an appropriate bounding cuboid was selected for each cell, whose volume (the volume of interest, VOI) depended on the actual size and shape of the specific cell under investigation revealed by SR101. VOI covered an imaging volume of (xyz range): 45-55 μm x 45-50 μm x 28 μm with 0.129-0.144 μm lateral resolution and 1μm axial resolution. In fast 3D experiments smaller VOI were centered on specific cell regions of interest (e.g., processes or end-feet). In these experiments, the average size of an imaged VOI was (xyz) 30 μm x 22 μm x 8 μm for processes, and 35 μm x 25 μm x 8 μm for end-feet. For cortical slice experiments, astrocytes were selected from the somatosensory region at a position and depth comparable to those of the experiments *in vivo* (see below for details). Imaging parameters, including acquisition rate and dimension of VOI, were also comparable to those used in imaging experiments *in vivo* and in hippocampal slices. For axonal stimulation experiments,

5

somewhat larger volumes were selected (typically 120 x 70 x 25 µm) at the expense of lateral resolution (0.2-0.3 µm per voxel). 3D + time images of single astrocytes were normally acquired at 2Hz (range: 1.5-2.2), i.e. with 28 individual two-photon focal planes scanned every 500 msec. In some experiments, the scanned volume was reduced and the acquisition rate increased up to 10 Hz. Typically, two 3 min-long acquisitions were made for each cell, spaced by 1 min interval, allowing for drift correction if needed. Two control measures were performed to exclude that significant photo-damage or induction of Ca^{2+} activity by laser occurred during our acquisitions: (a) comparison of mean frequency of the Ca^{2+} activity between runs 1 and 2, which showed no difference (P=0.44; paired t-test, n=14 cells); (b) check of whether overall GCaMP6f fluorescence intensity in the VOI slowly increased during acquisition periods, which also gave negative result. In some experiments the effect of Tetrodotoxin (TTX, 1 µM) was tested. The drug was bath applied for at least 10 min prior to recording (perfusion speed: 2ml/min). In these cases, two control runs were performed followed by the run in the presence of the drug. In other experiments, the effect of 4-aminopyridine (4-AP, 100 µM) was tested. The drug was bath applied for 10-15 min. Neuronal activity was monitored in parallel to astrocyte 3D Ca^{2+} dynamics, through a glass pipette electrode (resistance 5-8 MΩ when filled with aCSF) placed 20-30 µm away from the imaged astrocyte. Field signals were amplified, digitized at 20 kHz, and bandpass-filtered at 0.01- 80 Hz. The resulting trace was superimposed to the astrocyte Ca^{2+} imaging traces. For axonal stimulation experiments, the recording duration was increased to 15 min per acquisition (see below), and an additional 15 min-long recording was added for the TTX experiments.

Experiments in head-fixed awake mice were performed in the somatosensory cortex. Astrocytes were imaged at least 80 µm under the brain surface, and camera tracking of movements was generally combined. Similar to the experiments in brain slices, VOI covered an imaging volume of (xyz range): 36-43 µm x 36-43 µm x 20-35 µm with 0.121-0.144 µm lateral resolution and 1 µm axial resolution. Scanning rate was 1-3.3 Hz. The same astrocyte was imaged for 3-5 min (250-600 stacks) and, after 1 min of break, again for 3-5 min. Like in experiments *in situ*, we found no evidence of an increase in the frequency of Ca^{2+} events between run 1 and 2 in any of the analyzed astrocytic regions (soma: P=0.4; processes: P=0.9; end-feet: P=0.9; n=3 cells). In addition, no slow increase in fluorescence intensity throughout the GCaMP6f channel was observed during the time series. In the experiments conducted under anesthesia, isoflurane (2%) was administered in O_2. In a few experiments, the same cell was imaged before and after isoflurane administration.

3D Ca^{2+} imaging data analysis

The big data generated by 3D two-photon imaging (3-7GB per acquired cell) were processed thanks to the in house development of a dedicated analytic framework written in MATLAB for analysis and requiring Imaris 8.2 for visualization. To start, when drift was present, correction in xyz (3D translations) was performed taking into account the morphological channel (SR101 stacks) and using a mean square error minimization approach. The same transformation was consequently applied on the other channels. For acquisitions *in vivo*, recording time with movement >1 µm axial or in y-x, usually seen as a peak or a drop in the SR101 morphological signal, was excluded from analysis. If movement was limited to 1 or few frames, Ca^{2+} events in that period were considered empirically (e.g., counted for frequency measures but excluded from more precise measures, such as maximal volume spread). In order to reconstruct as much precisely

as possible the 3D structure of each recorded astrocyte, average time projections of both SR101 and GCaMP6f fluorescence were used for segmentation. In particular, SR101 time projection revealed accurately the structural "core" of the astrocyte, whereas GCaMP6f time projection revealed all the calcium-active parts of the astrocyte during the recording period, including the gliapil. Quality of the time projection was confirmed by comparison with high signal-to-noise, high-resolution z-stacks that were acquired at the end of every Ca^{2+} imaging session. Segmentation of each isolated astrocyte was performed by keeping all the voxels with intensity higher than average background value obtained from VOI regions devoid of any astrocytic structure. The structural core of the astrocyte was separated from the gliapil by using semi-automatic thresholding, based on 3D connected filters under user supervision, and further sub-divided in macro-regions: soma, stem processes with their structurally-resolved ($\geq$1 µm) appendages, end-feet. Ca^{2+} signals in the structural core of the astrocyte were extracted via what we called the "core segmentation method". The core structure was automatically divided into sub-regions (SR) using a 3D geodesic distance of 1 to 3µm of increment, depending on the experimental dataset (in particular, 1 µm increments were used for fast end-feet imaging, and 3 µm steps in all the other experiments). In every SR, $\Delta F/F$ calcium signals were computed as the spatial mean intensity at each different time point (FSR(t)) subtracted by the mean (mSR) of FSR(t), and normalized by mSR: (FSR(t)- mSR)/mSR. Ca^{2+} events were automatically detected, under user supervision, by means of the dynamics of regional maxima to detect peaks in every trace independently (*14*). Peaks of two contiguous SRs were automatically assembled into larger Ca^{2+} events based on their 3D connectivity and if they occurred within <3s one from the other. For each event, amplitude (from baseline to peak), duration (full-width half-maximum, FWHM), rise- time (from 10% to 90% of the peak amplitude), decay-time (from 90% to 10% of the peak amplitude), spreading distance (number of geodesic SR involved) and maximal volume spreading were automatically extracted and checked by the user. The hotspot event spread (total number of SR involved) was calculated only for those events involving the local hotspot regions of each process, defined as the subregion with the highest number of events detected over the entire recording time. Information about Ca^{2+} events occurring in the core of all the recorded astrocytes was registered in a database allowing rapid extraction of parameters related to events involving specific macro-regions. In practice, the maximum value for all the here-above parameters was used in each SR of a given macro-region involved in an event. As a result, events were classified into spreading versus non-spreading ones. Moreover, events were sub-classified as "fast" or "slow" if their duration in a given macro-region was <1.5s or $\geq$1.5s (FWHM). Due to the movement issue, this analysis could not be performed comprehensively in cells from the *in vivo* preparation. In order to get quantitative information on the ongoing Ca^{2+} activity throughout the astrocyte, i.e. including also in the structurally unresolved gliapil, we developed a second analysis approach, that we called "structure-free method". 3D Ca^{2+} activity throughout a segmented astrocyte, i.e. in the entirety of voxels having an intensity higher than the average background value, was computed voxel-wise as the frequency of changes of $\Delta F/F$ GCaMP6f fluorescence signal above threshold (inactive to active transition of a given voxel). Threshold was fixed in 3 to 4 standard deviations for experiments in situ and in 2 to 3 standard deviations for experiments *in vivo*. In some experiments, this was preceded by Gaussian filtering in time (1σ) and followed by spatial rescaling at 1µm per voxel in xyz with tricubic interpolation (see below). Data were expressed as mean voxel frequency. First, voxel frequency was calculated for each individual voxel, by dividing the number of inactive to active transitions of the voxel by

7

the duration of the recording period. Mean voxel frequency was then calculated as the mean of all the individual voxel frequency values in the segmented astrocyte. Mean voxel frequency values were obtained also for specific macro-regions/compartments (core, gliapil, soma, processes, and end-feet) by averaging individual voxel frequencies in the specific macro-region of interest. Comparison of mean voxel frequencies in core and gliapil required normalization by volume fraction because of the different nature, homogenous (core) versus spongy (gliapil), of the two macro-regions (see Ref. (*51*) and method of morphometric analysis). Additional analyses were performed to address specific aspects of the study by use of either one of the two methods or a combination of them. Estimation of the % of the total 3D Ca^{2+} activity in an astrocyte that would be reported by a single two photon focal plane (1 µm) was calculated by dividing the mean voxel frequency in the given focal plane by the mean voxel frequency in the full astrocyte. For this comparison, the best 2D focal plane was selected, defined as the focal plane including the highest amount of astrocytic activity. Ca^{2+} event frequencies in the astrocyte core were classified based on the macro-region/compartment of the event into process, end-foot and soma. Events spatially spreading in two or more macro-regions (processes count individually) were counted 1 in each of the macro-regions. The number of events attributed to a given macro-region was expressed as % of the total number of events counted in all the macro-regions during the acquisition time. Comparison of event frequencies in the different macro-regions in astrocytes of hippocampal slices versus cortical astrocytes *in vivo* required normalization of frequencies per number of subregions in processes and number of end-feet (size being more homogeneous for end-feet) recorded in the two preparations. Distribution of Ca^{2+} activity in each process was obtained by rescaling at 1µm per voxel in xyz and extracting the activity value (voxel frequency) for each voxel together with its 3D geodesic distance from the soma. By this, the activity level every 1µm away from the soma could be reconstructed and used to identify the average size of hot and cold regions within each process. In parallel, the % of process volume expressing a given activity level was calculated. Maximal volume spread and total duration of Ca^{2+} events involving the somatic region were extracted with the structure-free method upon spatial rescaling at 1µm per voxel in xyz. To calculate the volume, we considered the sum of the total number of spatially connected active voxels involved in each event; to estimate the total volume of global events *in vivo*, gliapil volume was corrected by volume fraction. To calculate the duration, the total active period from the start (first active voxel/s) to the end of each event (last active voxel/s) was considered. Study of synchronicity of the activity between two end-feet or between an end- foot and its process was performed by considering the peak amplitude of two Ca^{2+} events in the two different regions: if their peaks occurred <3 seconds apart, the two events were considered as synchronous. In addition, for the coordinated activity between an end-foot and its process, events needed to occur in anatomical continuity.

"Lead-lag" time delay correlation analysis

To understand the spatio-temporal evolution of "global" Ca^{2+} events, GCaMP6f-expressing astrocytes were recorded *in vivo* at high speed but lower voxel count (generally by reducing the number of z-planes). Next, a temporal cross-correlation was performed on the Ca^{2+} traces extracted from each voxel, vs the average Ca^{2+} activity across the entire volume containing the global Ca^{2+} event. This was used to assign a temporal delay value to each voxel as compared to the global population. Next, each voxel was color-coded according to the relative time offset of the lag bin

8

with the maximum cross-correlation value and assigned either to the "leader" or the "lagger" category. For lead-lag analysis on global events, neighborhood cross-correlation was normalized by subtracting the means of both the voxel and the global-average traces, and diving by their standard deviations. Unlike for the electrical cumulative cross-correlation calculation (see below), the individual time lag bins were not averaged. In a few cases, we have applied additional threshold, discarding any voxel whose maximum bin correlation was below an arbitrary value (e.g. 0.20): this resulted in larger fragmentation ("patchiness") of the maps, but did not produce a qualitative change in the spatial distribution of the lead/lag zones around the astrocyte, and is therefore not presented.

Axonal stimulation experiments

Ca^{2+} responses in DG astrocytes were evoked via targeted threshold stimulation of fluorescent (tdTomato or jRCaMP1a) PP axons. Brief current pulses (100-300 µs, 30 µA) were delivered focally to segments of the axons via a monopolar glass electrode (patch pipette, 4-6 MΩ when filled with aCSF) with the tip covered by fluorescent Quantum Dots (52), positioned ≥40 µm away from the imaged astrocyte to avoid any direct activation. This stimulation strength typically produces minimal synaptic activation in a postsynaptic neuron (35, 53). The axonal stimulation protocol consisted of 1 to 5 pulses (paired at 50 ms), delivered every 20 seconds. To discriminate the evoked and spontaneous Ca^{2+} activity of an astrocyte, stimulation periods (2-3 mins) were interposed with "rest" periods of the same duration. 3D Ca^{2+} data over time were collected at a typical throughput rate of 250 Mbps, corresponding to about 60 GB of data for a typical (30 min) duration of each recording. These Ca^{2+} data were acquired using a commercially available acquisition system externally synchronized to a separate electrophysiology system. The latter performed extracellular field recording and/or axonal stimulation via pClamp/AxoScope 10.3 software driving digitizers linked to the amplifier, constant current stimulator, and also receiving the Y-galvanometer feedback position from the imaging system. The Y-galvo position output pin was sending the 3D + time stack frame count, including the realtime Y-scanline position for each frame, and was continuously sampled at 1 kHz by the electrophysiology setup throughout the experiment. In this fashion, the exact relative timings of each current pulse and each 3D frame were available for correlation analysis. Detection of the stimulation-activated astrocytic Ca^{2+} responding regions in the 3D volume of the astrocyte was accomplished post-hoc via a specially developed ImageJ (NIH) software plugin (available from Volterra lab). Briefly, for each of the 3D voxels, a response index was calculated by performing a modified normalized cumulative cross-correlation between the voxel's Ca^{2+} signal time series and an electrical stimulation trace on a short (4-7 s) lead/lag window. To compensate for the jitter present in the onset of astrocytic Ca^{2+} responses, cross-correlation coefficients for all the positive values of lag were summed up. The corresponding formula for this calculation is as follows:

$$\text{NCCC}(x, y, z) = \frac{1}{w} \sum_{l=0}^{w} \sum_{t=0}^{d-w} \frac{\left(m_{t-l}(x, y, z) - \overline{m}(x, y, z)\right) \cdot n_t}{\sigma_{m(x,y,z)}}$$

where CC is the normalized cumulative cross-correlation coefficient for each voxel centered at coordinates (x, y, z), mt is the calcium trace and nt is a binary transform of an electrical stimulator

input at time t, w is the length of the cross-correlation window, and d is the duration of the acquisition in sample points. Following the calculation, the CC values for each voxel were thresholded to indicate the actively time-locked "responding regions" of the astrocytic structure. The responses were verified by placing VOIs and overlaying the extracted Ca^{2+} and input stimulator traces. Furthermore, when the image data were cross-correlated to the "scrambled" electrical input trace, this produced a much lower number of significantly correlated voxels (Fig. S11A). For the dual Ca^{2+} indicator experiments (Fig. 7C), we expressed jRCAMP1a in PP axons, and GCaMP6f in astrocytes. Both fluorophores were simultaneously excited at 965 nm, and the acquired red and green signals were analyzed in ImageJ. Because axonal Ca^{2+} transients were weaker, this necessitated a larger oblong VOIs traced along a short stretch of the putatively activated axon, placed immediately adjacent to the astrocytic VOI. To maximize effective ΔF/F for jRCaMP1a, we reduced background slice fluorescence by omitting incubation with red morphological dye SR101 prior to functional Ca^{2+} measurements, but instead visualized astrocytic morphology by post-loading the slice with a higher SR101 concentration via a perfusion system at the end of the recording (500 nM solution perfused at 3 mL/min at 34 °C, for 20 minutes).

In a set of control experiments, we evaluated the neuronal responses to axonal stimulations using protocols identical to those of the astrocyte experiments. In particular, we evaluated the percentage of neuropil volume that responded to axonal activation. Mice carrying the floxed GCaMP6f gene were injected with a neuronally-targeted AAV5.CamKII:Cre virus, leading to neuronal expression of the Ca^{2+} indicator. The relative size of the responding neuropil regions was calculated as done for the reliably responding regions of astrocytes. For experiment in Fig. S10B, two HFS pulses were added to the stimulation protocol to weakly highlight the general direction of the maximally-reachable neuropil regions.

<u>3D morphometric analysis</u>

Acute brain slices from P30-P40 *GFAP-EGFP* mice (*44*) were imaged with two-photon setup 2 at a resolution of 0.05 x 0.05 x 0.5 μm^3 (xyz) over 50-80 µm, axially centered on a given astrocyte in order to acquire its entire structure. Only EGFP-expressing astrocytes not surrounded by any other fluorescent astrocyte and therefore displaying an unambiguously identifiable structure were selected. Three-dimensional images of the astrocytes acquired in the CA1, CA3, DG hippocampal regions and in the somatosensory cortex were analyzed with custom made programs written in MATLAB (MathWorks Natick MA USA), and visualized with Imaris 8.2 (Bitplane, Switzerland). EGFP-expressing astrocytes were segmented by keeping the voxels having an intensity higher than the average background value (i.e. where there was no astrocytic structure). The structural core part of the astrocyte, including cell soma, end-feet and stem processes with appendages up to structural elements ≥1 µm that could be visually identified at optical resolution, was separated from the structurally unresolved gliapil by using semi-automatic thresholding under user supervision, allowing to define the soma, main processes and end-feet. Gliapil was defined as the segmented astrocytic parts which were not in the core. Gliapil volume was corrected by volume fraction (VF) from the core (*51*). Thus, the intensity value of each voxel within the gliapil was divided by the average intensity within the core to obtain the VF for all the voxels. The volumes were defined as the sum of all the VF of all the voxels within the core (containing 100% of astrocytic structure: VF =1) and gliapil multiplied by the physical size of a voxel. For each 2D vs 3D comparison, the "best 2D" focal plane, i.e. the plane containing either the biggest amount of

10

astrocytic structure, or the biggest number of end-feet or processes, or the longest process length (calculated as the longest path amongst all the possible bifurcations from the soma to the smallest resolvable branch), was automatically found in every possible slice of 1µm thickness and divided by the corresponding total quantity in 3D. For morphometric quantification of axonal linearity, images of individual tdTomato-fluorescent PP fibers in the hippocampal DG were acquired using VOIs with increased lateral (up to ~0.06 µm) and axial (0.5 µm) resolution and temporal averaging. Axonal fibers were semi-automatically traced in xy and lz projections using NeuronJ plugin (*54*) and a custom written ImageJ script. The resulting 3D coordinate files were analyzed for lateral and vertical deviation from the principle layer (bulk) fiber direction. For cases of high fiber density, individual fiber signals were pre-segmented in 3D using a custom ImageJ plugin before tracing (available from Volterra lab).

<u>Statistics</u>

For all statistical analyses, Matlab, Origin 8, GraphPad Prism 6, and Excel were used. Data were generally expressed as mean value ± SEM and considered as significantly different when the p value was less than 0.05. Unpaired t-tests or rank sum test were used when comparing the means of two independent experimental populations (e.g. properties of Ca2+ events such as duration, or categories, data ex vivo vs. in vivo), whereas paired t-test or signed rank test were used for comparing interdependent populations (e.g., Ca2+ activity between runs 1 and 2, events in 2Hz and 10 Hz acquisitions). For 3D morphometry statistical comparisons were made using paired non parametric Kruskal-Wallis' test or with Wilcoxon rank sum test, depending on the type of comparison.

Table S1. Properties of the Ca²⁺ events detected in the core regions of GCaMP6f-expressing astrocytes in acute hippocampal slices*.

Astrocyte Region †	Amplitude (ΔF/F)	Duration (FWHM, s)	Rise time (s)	Decay time (s)	Volume (µm³) §	Spreading distance ¶	N-value (events)
Processes	2.33 ±0.05	2.64 ±0.07	2.58 ±0.10	4.33 ±0.19	47.93 ±2.08	2.11 ±0.06	567
End-feet	1.93 ±0.14	2.94 ±0.28	2.36 ±0.29	4.53 ±0.73	90.77 ±12.88	1.66 ±0.13	65
Soma	2.18 ±0.27	5.13 ±0.44	4.50 ±0.46	8.16 ±1.17	478.51 ±17.99	4.91 ±0.31	34

* Ca²⁺ events detected using GCaMP6f as indicator, 2Hz as speed of volumetric 3D two-photon imaging acquisitions and analysis performed with "core segmentation method" as described in Methods. Care should be taken when comparing the event parameters reported in this Table to those obtained in other studies using different acquisition modes (e.g., incomplete 2D/confocal), different Ca²⁺ sensors (e.g. slower GCaMP3/mGCaMP3), different acquisition speeds (much slower or faster than 2 Hz), and different analysis approaches.

† Astrocytic regions defined by segmentation of the astrocytic core according to live SR101 staining. Within regions, sub-regions defined by segmentation of the region in equal geodesic distance increments away from the center of the soma, step size: 3 µm.

§ Ca²⁺ event volume is calculated as the total volume of all the individual sub-regions involved in the event. Please note that these values have a "quantal" resolution of one sub-region, and true event volumes may in reality be smaller as an event could occupy just portions of its extreme sub-regions. Also, notice that average sub-region volumes are different in different astrocytic regions: 21.14± 0.73 µm³ in processes, 51.75± 6.64 µm³ in end-feet, 83.90±7.05 µm³ in soma. End-feet sub-region volumes overestimate real volumes because the SR101 signal does not permit exact dissection of the end-foot enwrapping a vessel from the vessel structure itself.

¶ Spreading distance is defined as the number of contiguous sub-regions involved in each event. For soma, sub-regions were defined as "tangerine" segments.

Abbreviations: FWHM, full width duration at half-maximum amplitude; s, seconds,
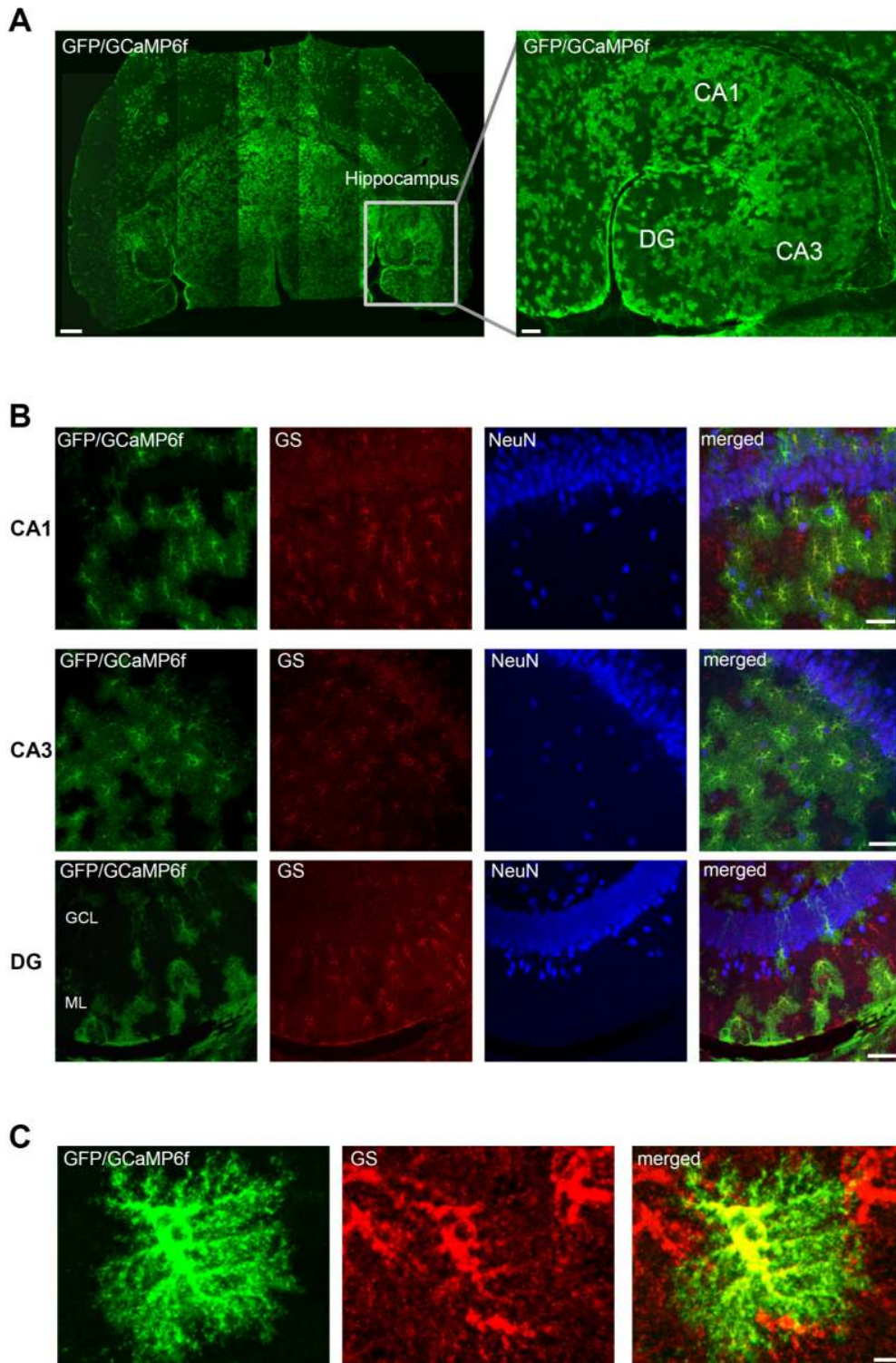
Supplemental Figures S1-S11:

Fig. S1. Characterization of *GFAPCreERT2xGCaMP6f* mice with immunohistochemistry.

(A) *Left*: 7x5 combined confocal images show the horizontal brain section of a 39 days-old mouse taken 15 days after the first tamoxifen injection. GCaMP6f expression is present throughout the brain (green, GFP/GCaMP6f: GCaMP6f labeled with anti-GFP antibody). Scale bar: 500 μm. *Right*: zoom-in of the hippocampal region shows patchy distribution of GCaMP6f expression hinting already to an astrocyte-specific pattern (DG: dentate gyrus; CA1 and CA3: cornu ammonis 1 and 3). Scale bar: 100 μm. **(B)** Astrocyte-specific expression of GCaMP6f in the CA1, CA3 and DG hippocampal regions. From left to right, staining with: GFP for GCaMP6f (green), glutamine synthetase (GS, red) as astrocyte marker, NeuN (blue) as neuronal marker, and overlay of the three (maximum intensity z-projection from four to eight 1μm-thick confocal stack acquisitions; scale bar: 50 μm). Astrocyte-specificity is 100% in CA1 and CA3 (n=79 cells in CA1; 97 in CA3), whereas is 90% in DG (n= 90 cells), where a minor population of neural precursors/immature neurons (9 cells neither GS-positive nor NeuN-positive and 1 cell NeuN-positive) are labeled together with astrocytes. **(C)** GFP labelling reveals homogeneous and widespread GCaMP6f expression throughout the structure of an astrocyte. From left to right: 3D view of a 29μm confocal stack of an astrocyte as revealed by GFP/GCaMP6 labeling (green), GS labeling (red) and their overlay. The GECI expression seen in this astrocyte in isolation from neighboring ones, covers the astrocyte volume beyond the structures revealed by GS staining and is therefore valid for reporting Ca2+-activity from throughout the astrocyte, including the optically less resolved regions like the gliapil. Scale bar: 5 μm.
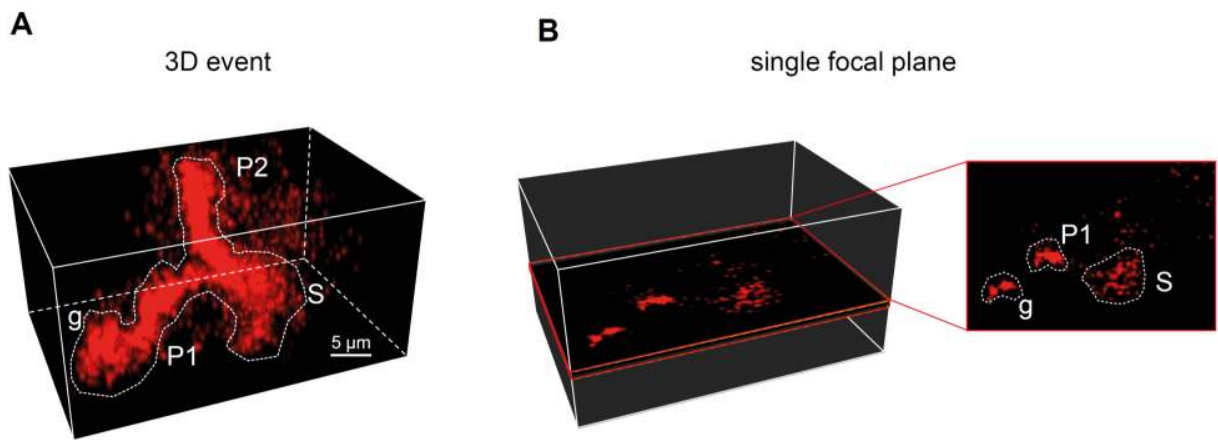
14

Fig. S2. Incorrect detection by 2D imaging of astrocytic Ca2+ events spatially spreading over multiple focal planes.

(A) In red, reconstruction of a complex three-dimensional Ca^{2+} event encompassing two processes (P1, P2), the soma (S), and parts of the gliapil (g). The event spreads over multiple focal planes (dimension of imaged VOI: 42 x 28 x 21 µm). **(B)** This single event would be incorrectly reported by 2D imaging in a single focal plane, even in the best plane: first, the event would be seen as three smaller unconnected events, one in the gliapil, another one in P1 and a third one in the soma, with errors in both event frequency and spatial spread. Second, the parts of the event spreading to the second process (P2) would be entirely missed with a further error in the spatial spread of the event.
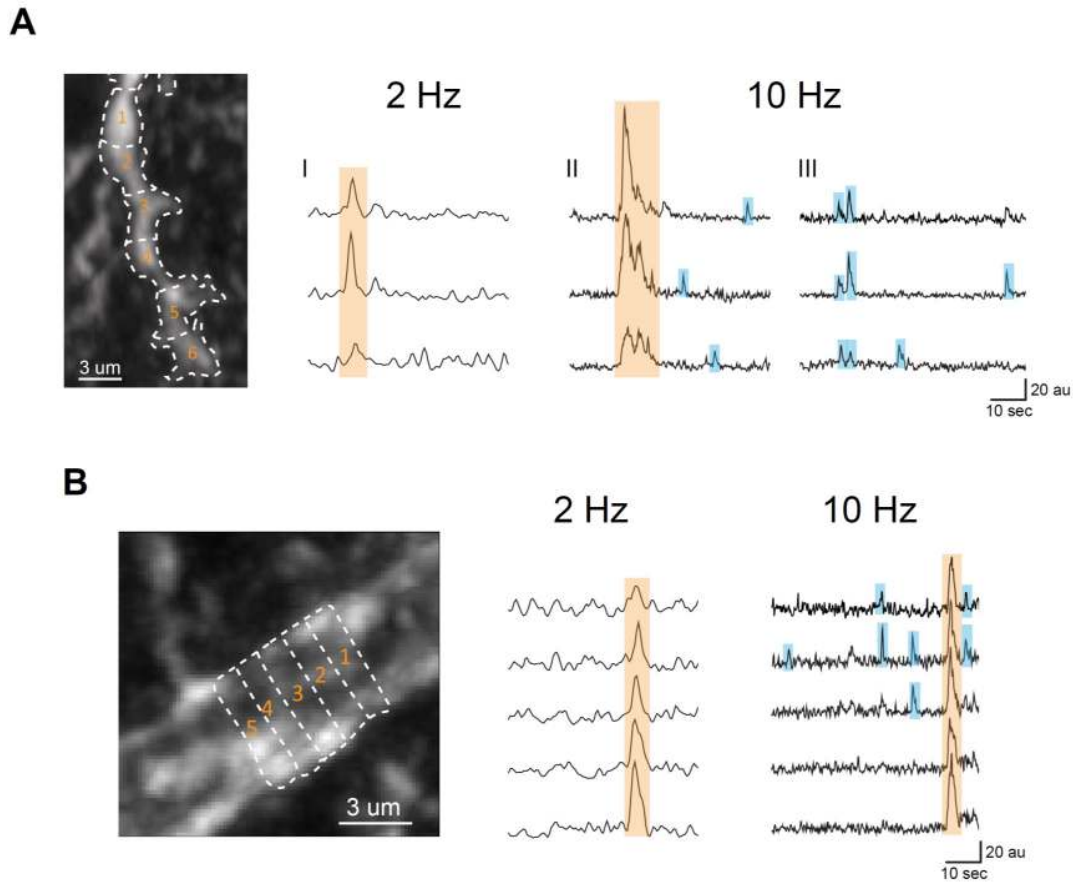
Fig. S3. Increasing 3D acquisition rate permits detection of faster Ca^{2+} events in astrocytic processes and end-feet.

(**A**) Ca^{2+} activity detected in a single process imaged in 3D at either 2 Hz or 10 Hz. The core structure of the process is revealed by SR101 loading (in grey, time projection over the whole imaging period) and, in both types of acquisition, is segmented in consecutive sub-regions of 3 µm length (1-6). Ca^{2+} traces from groups of neighboring sub-regions (SR) are shown (group I = SR 2-4, starting from the top trace; II = SR 3-5; III = SR 4-6). For each group, Ca^{2+} traces were selected by cropping representative stretches of activity during acquisitions recorded at either 2 Hz (group I) or 10 Hz (groups II and III). Events are highlighted with different color-codes according to their features. Ca^{2+} events with duration ≥1.5 sec (FWHM, orange highlight) were captured at both 2 Hz and 10 Hz, but sampling at 10 Hz revealed the additional presence of a population of faster and smaller events, often restricted to one or few SRs (light blue). (**B**) Ca^{2+} activity detected in an end-foot imaged at either 2 Hz or 10 Hz. The end-foot structure is revealed by a combination of SR101 and GCaMP6f signals projected over the entire recording time and divided in consecutive sub-regions of 1µm length (1-5). Ca^{2+} traces from each of the 5 sub-regions during the 2 Hz and 10 Hz acquisitions are comparatively shown and fast and slow events are highlighted with the same color code as in (A). Slow events, visible at both 2Hz and 10 Hz, occupy most of the end-foot structure, whereas fast events, revealed only at 10 Hz, remain confined to just one or few sub-regions, i.e. to fractions of an individual end-foot.
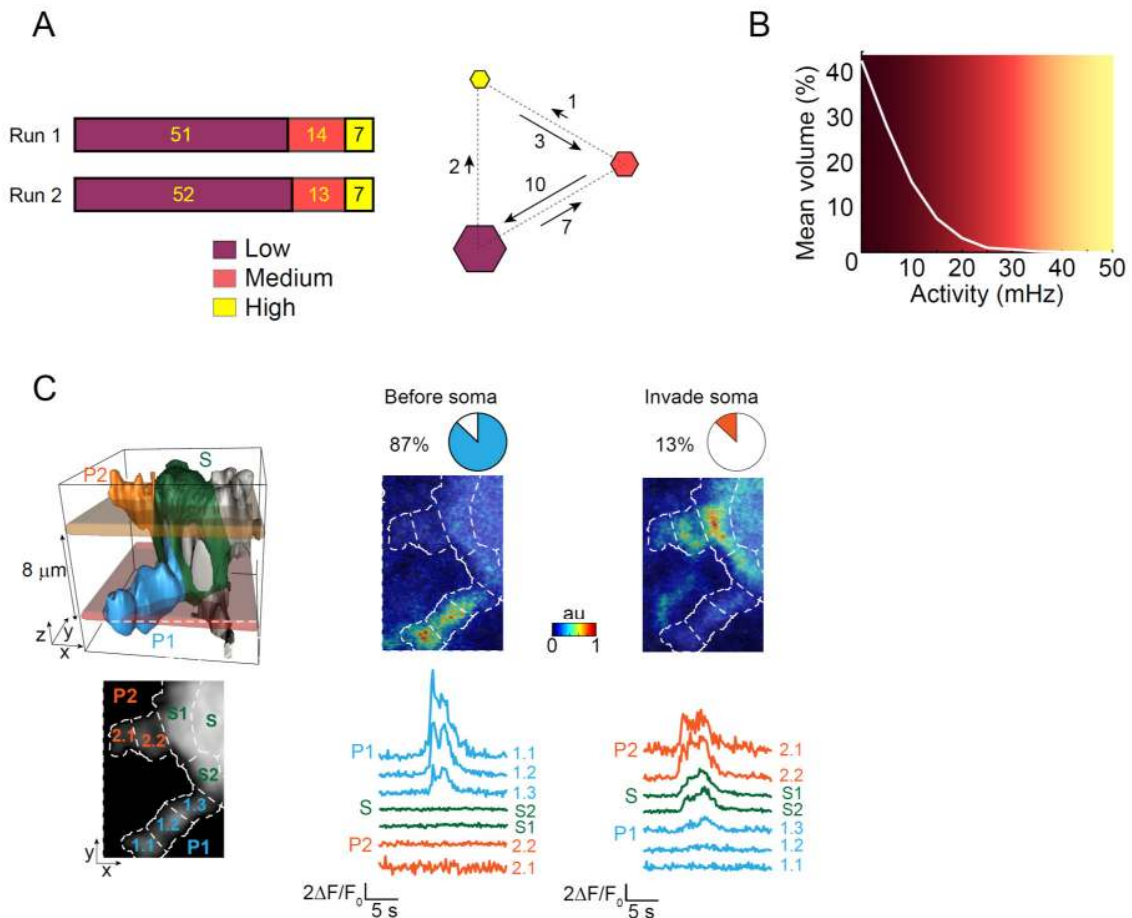
16

Fig. S4. Ca^{2+}activity in astrocytic processes: analysis of stability over time, frequency per process volume, and likelihood of somatic spread.

(A) Analysis of stability over time. *Left:* Bars show the total number of low, medium, and high activity processes (see Fig. 4A) in two consecutive 3 min-periods of recording (runs). Proportions remained basically the same in Run1 and Run 2. *Right*: number of individual processes that transitioned between activity levels (same color coding than on the left): transitions are indicated by the numbers adjacent to each arrow (e.g., in the second run, 7 processes went from the low to the medium level, whereas 10 other processes went from the medium to the low activity level). **(B)** Graph showing distribution of activity (in frequency) with respect to process volume (in %). Frequency is calculated in 1 μm^3 domains in every analyzed process (see Fig. 4C,D). **(C)** Likelihood of somatic spread of Ca^{2+} events originating in astrocytic processes. *Left*, *top:* representative morphological reconstruction of an astrocyte in which we performed 3D monitoring of activity in two processes (P1 and P2) adjacent to the soma (S). *Bottom:* all the P1, P2 and S sub-regions from which we monitored activity. *Middle:* pseudo-color example and corresponding traces of an event in P1 that terminates at the interface with S. *Right:* example of an event in P2 that enters the soma but does not spread from this beyond the interface with P1. These experiments revealed that most of the process events terminate in the interface region before the soma, and only a minority actually invades at least one somatic region.
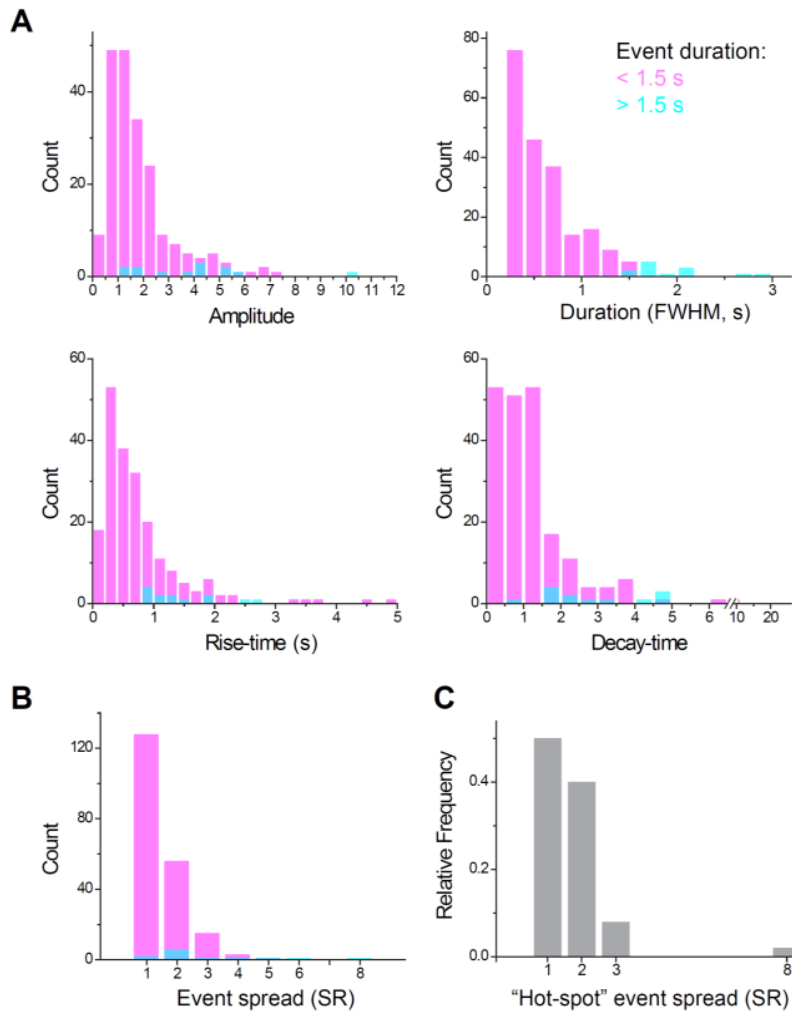
17

Fig. S5. Fast-rate volumetric 3D scanning in astrocytic processes: distribution analysis of the Ca²⁺ event parameters.

In these experiments, the sampled volume was reduced (in z-depth and linear dimensions) to contain just an individual process (see Results); the sampling rate was correspondingly increased to 10 Hz. These experimental conditions revealed the presence of a prevalent sub-population of fast and small Ca^{2+} events not captured in routine 2Hz acquisitions. Analysis performed on 216 Ca^{2+} events from 8 processes in 4 cells. **(A)** Distribution of event properties (amplitude, duration, rise- and decay-time). Magenta color-code denotes "fast" events (FWHM: <1.5s), and cyan "slow" events (FWHM: >1.5s). **(B)** Distribution of spatial event properties. Event spread expressed as number of individual sub-regions (SRs) involved in the event (SRs drawn geodesically along the principal process axis away from soma, in 3 µm increments; average SR volume: 26.17± 2.28 µm³). Most events were confined to 1 or 2 SRs; **(C)** Spatial event properties, but restricted to Ca^{2+} events occurring in the "hot-spot" region of each process, i.e. the region showing highest event frequency (see Fig. 4D). Like events in other regions, "hot-spot" events were mostly confined to 1 or 2 SRs, with a somewhat higher percentage of 2 SRs events.
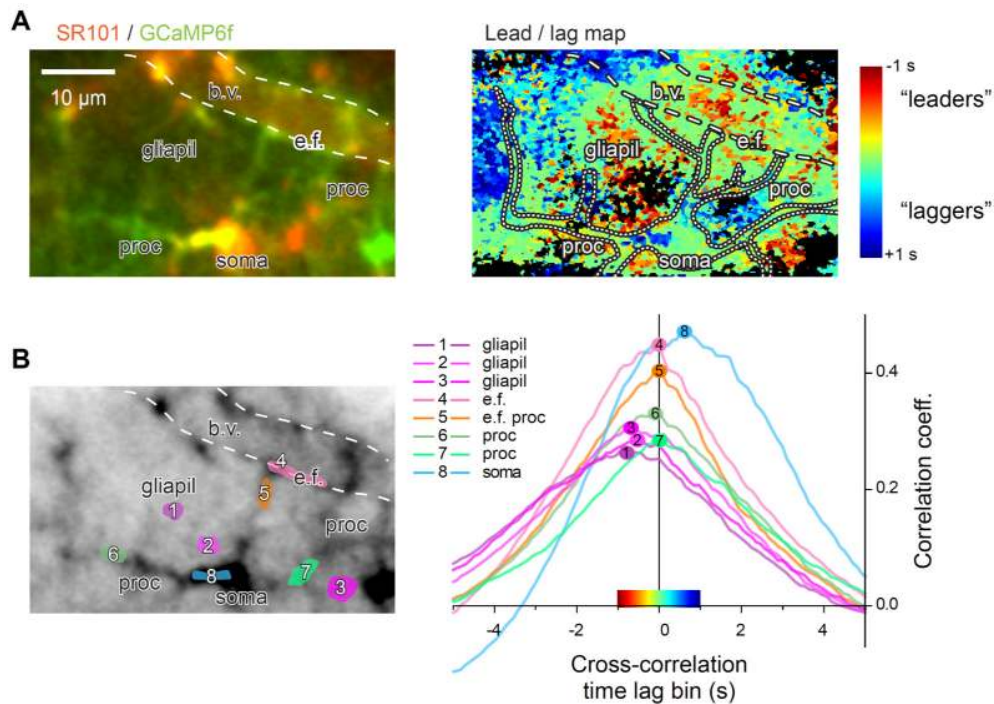
18

Fig. S6. Lead-lag cross-correlation analysis of astrocytic Ca^{2+} signals reveals multifocal decentralized nature of global events *in vivo*.

To study the temporal sequence of fast-developing "global" events *in vivo*, we recorded in few experiments selected parts of GCaMP6f-expressing astrocytes (7 continuous z-frames) at high temporal resolution (10 Hz) and performed a voxel-wise normalized cross-correlation analysis vs the entire event GCaMP6f signal (see Methods). **(A)** *Left:* combined morphological (SR101) and cumulative GCaMP6 signals showing visible components of the imaged astrocyte, including soma, two generic processes (proc), an end-foot process terminating in an end-foot (e.f) contacting a blood vessel (b.v) and the surrounding gliapil. *Right*: normalized cross-correlation projection map wherein individual voxels are colored according to the temporal offset with respect to the time showing the strongest correlation (time lag bin with respect to the greatest correlation value). "Jet" colormap is shown to the side; earliest "leader" voxels are colored in tones of red, latest "lagger" voxels are colored in blue. In general, many small, physically disconnected, regions of gliapil seem to precede the average global event. This suggests a multi-focal origination nature of the "global" events, rather than a "wave" spreading from one side of the cell to another. **(B)** *Left*: gray-scale average GCaMP6f image indicating the placement of the manually drawn VOIs used to extract the average cross-correlation voxel profiles displayed on the right. *Right*: Normalized cross-correlation traces extracted from the voxels in the VOIs to the left. Several areas of the gliapil are "leaders" (VOIs 1-3, pink), and are activated with approximately the same advance despite being physically disconnected in space. Process regions and end-foot activate with minimal offset to the average global event (VOIs 4-7, pink, orange and green), and regions of the soma are significantly delayed (VOI 8, blue, "laggers"). For display purposes, a threshold discarding any voxel with maximum bin correlation <0.20 was applied (voxels below this value are set to black). The same threshold was applied in Fig. 4F.
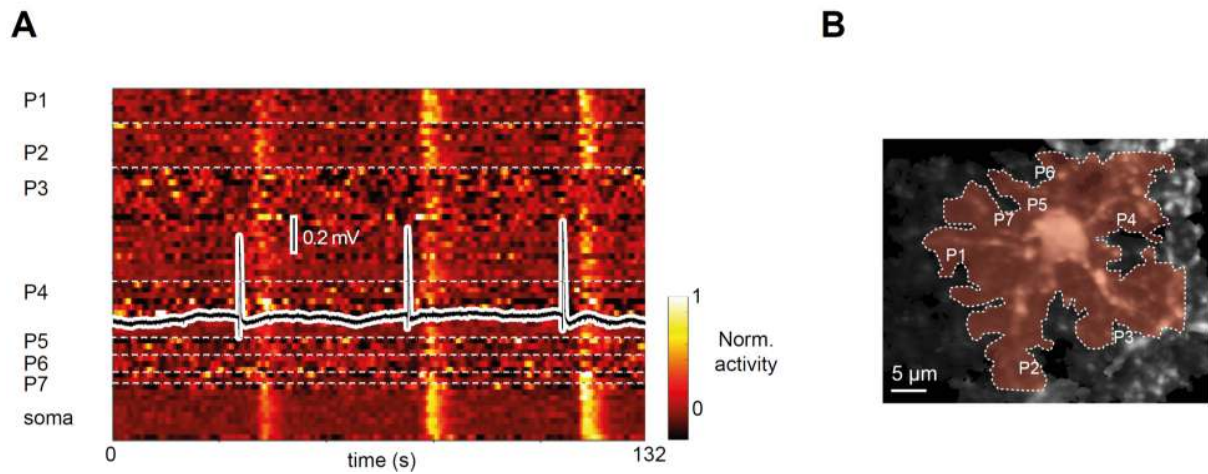
19

Fig. S7. Pharmacologically-induced intensified neuronal firing results in "global"-like Ca²⁺ events in hippocampal astrocytes in situ.

Acute application of the pro-epileptogenic drug 4-aminopyridine (4-AP, 100 µM) results in hypersynchronous neuronal activation in the hippocampus in situ within several minutes of application. **(A)** Representative raster plot of normalized Ca²⁺ activity in all the segmented regions of an astrocyte (P1-P7, processes; S, soma) over about 2 minutes with overlaid synchronized trace of the local field potential (LFP) recorded in the slice. Notice that each large change in the LFP is followed (within 2s) by a "global- like" Ca²⁺ event in the astrocyte. **(B)** Top down view of the same astrocyte visualized by SR101 loading. The overlay indicates the maximum spread of one of the "global"-like events.
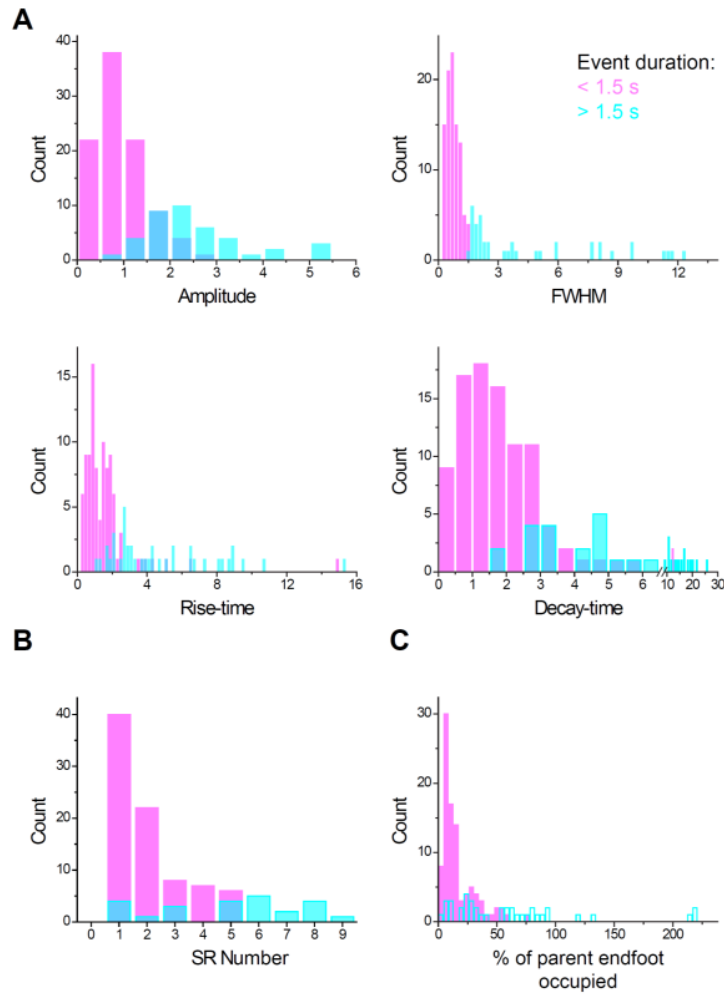
Fig. S8. Fast-rate volumetric 3D scanning in astrocytic end-feet: distribution analysis of the Ca²⁺ event parameters.

In these experiments the sampled volume was reduced (in z-depth and linear dimensions) to contain one to three end-feet (see Results); the sampling rate was correspondingly increased to 10 Hz. These experimental conditions revealed the presence of a large sub-population of fast and small Ca^{2+} events, often spatially confined to just a fraction of an end-foot, not captured in routine 2Hz acquisitions. Analysis performed on 136 Ca^{2+} events from 13 end-feet in 4 cells. **(A)** Distribution of event properties (amplitude, duration, rise- and decay-time). Magenta color-code denotes "fast" events (FWHM: <1.5s), and cyan "slow" events (FWHM: >1.5s). **(B)** Distribution of spatial event properties. Event spread expressed as number of adjacent end-foot sub-regions (SRs) involved in the event (SRs segmented orthogonally along the blood vessel in 1 µm steps; average SR volume: 16.99± 0.55 µm³. When multiple GCaMP6f-positive end-feet were present contiguously on the same blood vessel, their individual borders were determined visually by the experimenter. **(C)** Distribution of Ca^{2+} event sizes expressed as percentage of the parent end-foot volume. Most events were smaller than an individual end-foot. Values >100% represent synchronous multi-end-foot events.
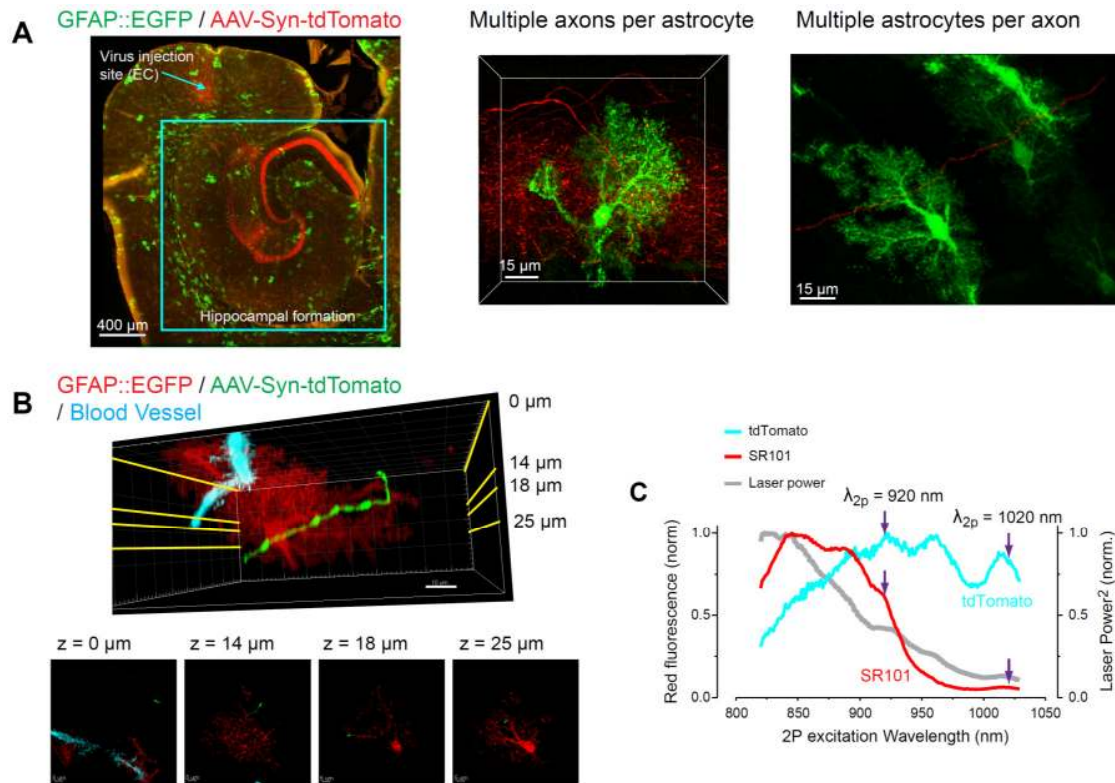
21

Fig. S9. 3D study of the complex morphological relationships between axons and astrocytes in the hippocampus.

(A) *Left:* Maximum projection image (45 µm in 9 z-steps) of the forebrain of a *GFAP- EGFP* mouse 4 weeks after injection of AAV-Syn-tdTomato into the entorhinal cortex (EC). Astrocytes are in green, PP axons in red, mostly straight en route (EC, subiculum) and highly convoluted at destination (e.g., DG molecular layer). This dual color approach permitted direct visualization of the complex astrocyte-axon morphological interactions reflecting potential functional interactions, including: *Middle*: multiple axonal fibers crossing a single astrocyte (see also Movie S4); *Right:* a single axonal fiber contacting multiple astrocytes (maximum projection image). **(B)** *Top:* Representative example showing an individual fluorescent axon (green) crossing the 3D territory of an astrocyte (red) and a blood vessel (blue) over multiple focal planes. For clarity, other nearby axons are masked. *Bottom:* the axon-astrocyte interactions as seen from four individual planes. None of them permits to understand the continuity of the morphological (and functional) interactions between this single axon and the astrocytic structures. **(C)** Two-photon excitation spectra of SR101 and tdTomato. To study simultaneously morphological and functional axon-astrocyte interactions in 3D, we used in combination SR101 (loaded at nanomolar concentration in astrocytes) and tdTomato (expressed in axons) in *GFAPCreERT2xGCaMP6f* mice: (see Figs. 6, 7). In spite of similar emission profiles, we could optically separate the two red reporters based on their different two-photon excitation properties. Alternatively, varying wavelengths between 920 (for SR101, left arrows) and 1020 nm (for tdTomato, right arrows), we could unambiguously assign structures to axons or astrocytes without need for any spectral unmixing or similar computational approaches.
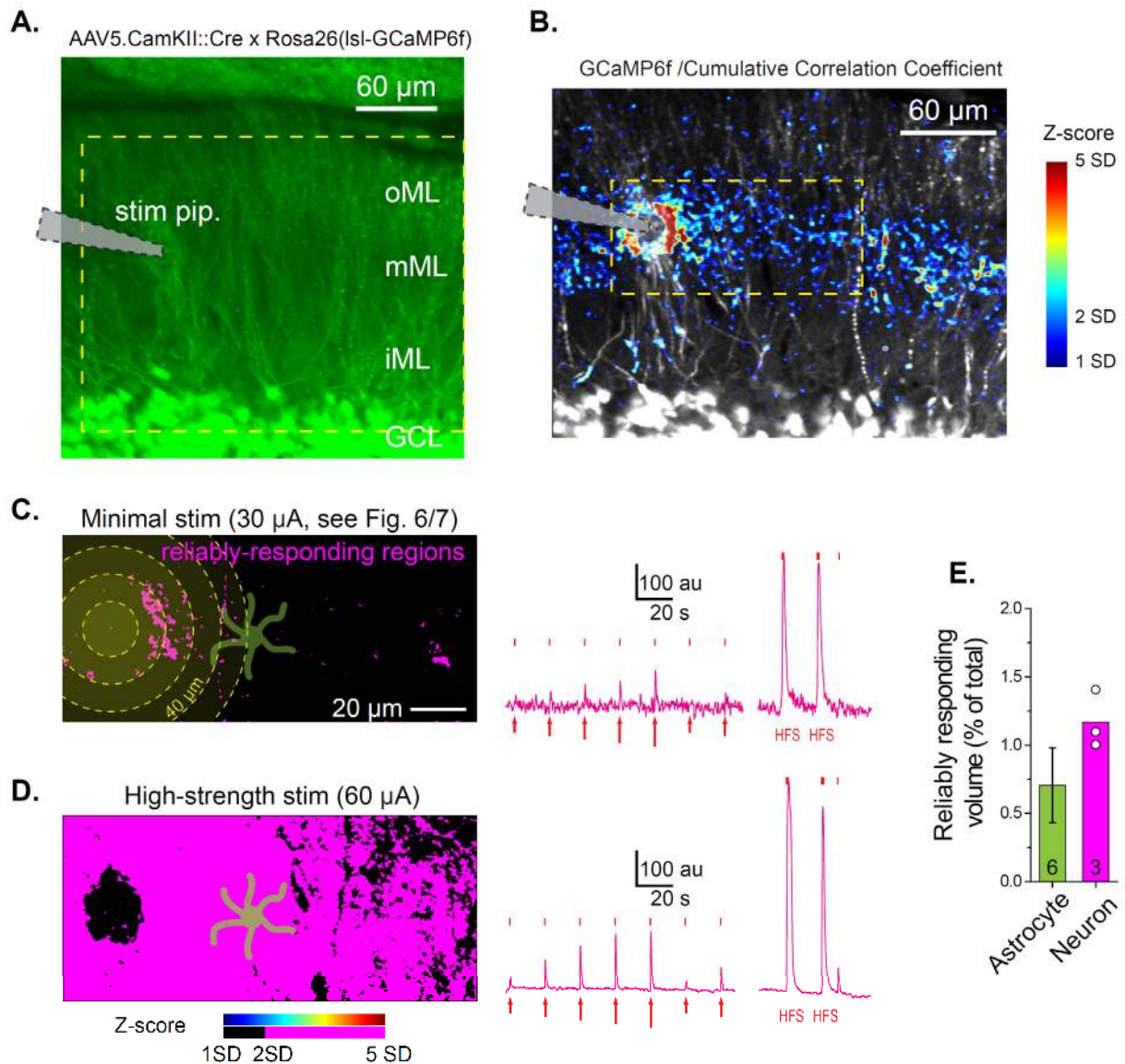
22

Fig. S10. Sparse neuronal Ca²⁺ response to minimal electrical stimulation of axons

Mice with floxed GCaMP6f were injected with neuronal Cre virus (AAV5.CamKII0.4.Cre.SV40) in the dentate gyrus (DG) to trigger GCaMP6f expression selectively in neurons. **(A)** Low-zoom average projection of a two-photon stack illustrating the arrangement for electrical stimulations in the DG. Morphological image processed with a square-root function. Dashed outline indicates the region shown in 2D (z=1µm) in B. (GCL, granule cell layer; o-m-i-ML: outer, medial, and inner molecular layer; stim pip: location of the stimulation pipette). **(B)** Response map produced by 19 "minimal stimulation" episodes (30 µA; 1-5 pulses, see Figs. 6,7 and Methods) augmented by two HFS trains (1s, 100 Hz). Average GCaMP6f signal in grayscale; corresponding cumulative cross-correlation (see Methods) in "Jet" colorscale as indicated to the right. Minimal electrical stimulations produced a low amount of time-correlated postsynaptic responses in the GCaMP6f-

positive regions >20 µm away from the stimulating pipette, visually resembling the expected pattern of axonal divergence in the medial perforant path layer. These sparse but persistent "responding regions" appeared to be the result of activating individual axonal inputs via evoked APs, pre-synaptic release, and post-synaptic activation. In contrast, strongly "responding regions" within ~10-20 µm from the stimulating pipette may be either the result of direct electrical stimulation and/or activation of multiple axons converging onto the same postsynaptic dendrite(s). **(C)** Distribution of the neuronal regions in the DG reliably responding to the protocols in B relative to distance from the stimulating pipette. *Left:* threshold-based ("magenta") cumulative cross-correlation response maps obtained in a single focal plane (z= 1µm) at 70 Hz. An astrocyte is overlaid for illustration purposes, i.e. to show the neuronal Ca^{2+} response in the region typically studied in axon-astrocyte interaction experiments (see Fig. 7). *Right*: Neuronal GCaMP6f signal extracted from reliably-responding regions >40 µm away from the pipette. Responses to minimal stimulation are proportional to the number of pulses (1-5 pulses indicated by arrow size); responses to HFS trains are much larger. Exact timing of each pulse is shown by tick marks above the trace. **(D)** Stronger, "high-strength stimulation" (60 µA) evokes massive time-locked GCaMP6f fluorescence response, 100-fold bigger than threshold stimulation (from 0.83 to 81.66% of the FOV at locations >40 µm), indicating that the small response in C is truly due to sparse neuronal activation, not to lack of GCaMP6f expression in neurons. *Right*: Neuronal GCaMP6f signals extracted from the distal (>40 µm away) reliably responding regions. **(E)** Comparison of the mean astrocytic and neuronal responding volumes to the same minimal axonal stimulation protocol. Experiments in astrocytes and neurons were performed separately. Data are from "before TTX" dataset in Fig. 7 for astrocytes, and from this figure for neurons (n=3 from 2 slices and 2 different animals). Overall, Ca^{2+} responses in both GCaMP6f-positive astrocytes and neurons are sparse and restricted to a minimal fraction of the imaged volume.
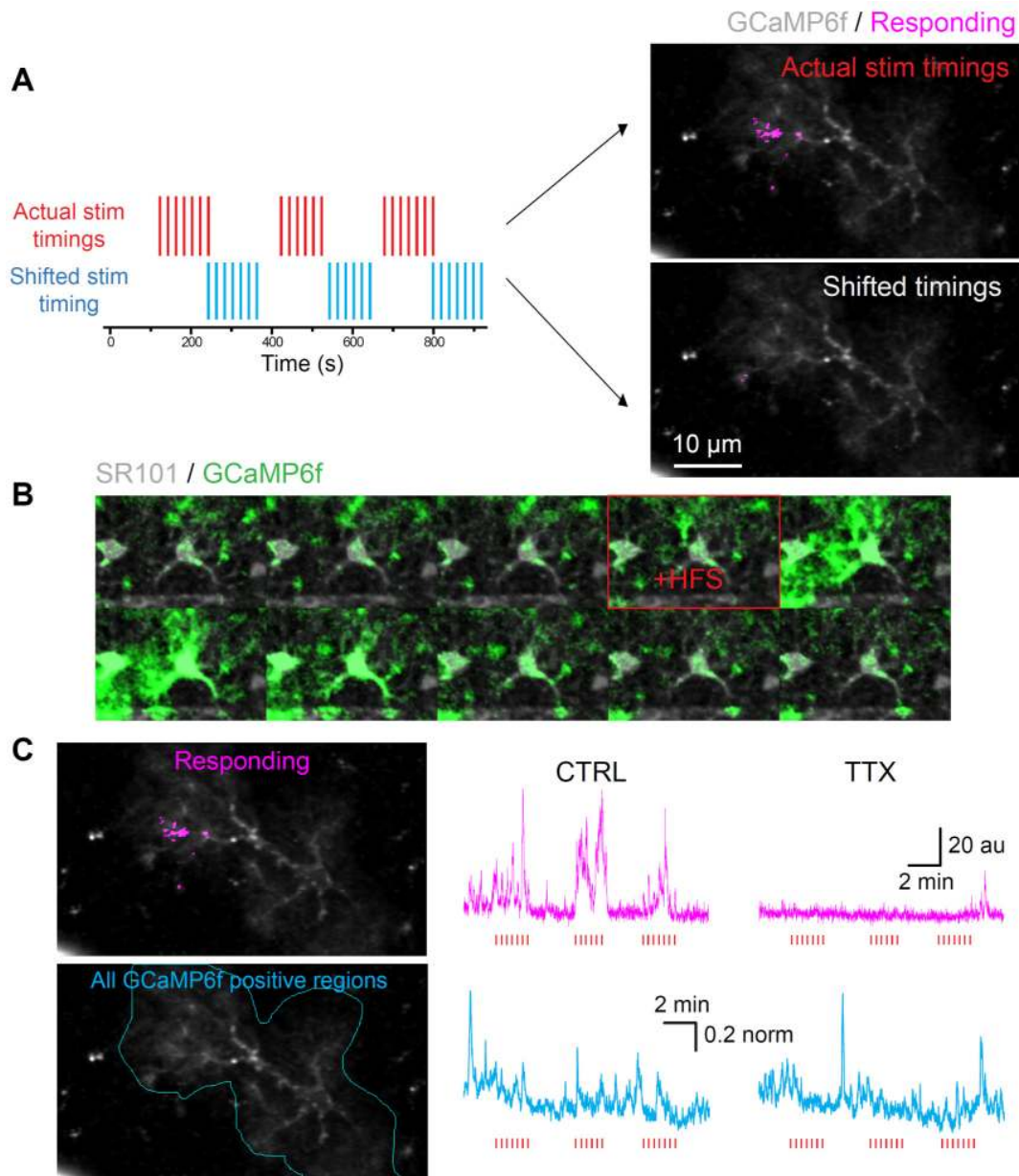
Fig. S11. Methodological issues in the study of the relationship between axonal firing and astrocytic Ca²⁺ responses.

(A) Validation of our computer-assisted detection of the responding regions within the total imaged volume of an astrocyte in minimal axonal stimulation experiments. Given the very large number of voxels encompassing the total imaged astrocyte volume in "blind" stimulation experiments, a potential problem of our normalized cumulative cross-correlation approach (see Methods) is that it may detect voxels correlated to the electrical stimulation purely by chance (the so-called "Million-monkey" problem). In order to control for such occurrence, we have generated shifted ("scrambled") electrical stimulation traces (*left,* blue protocol) that were fed into the

program together with the real Ca^{2+} imaging data, while keeping the positive correlation threshold and all other parameters intact. In all cases, the "scrambled" traces produced much fewer positively correlated voxels (*right*, bottom image) compared to the real stimulator data (*left,* red protocol; *right*, top image), and such "positive" voxels were randomly scattered throughout the structure. **(B)** The likelihood of positive detection of an astrocytic Ca^{2+} response to axonal firing is increased by the size of such response. The representative time-series of average projection images of the GCaMP6f signal shows the effect of tetanic axonal stimulation (HFS) in inducing a large, "global-like" Ca^{2+} response in the astrocyte spreading over most of its structure and across multiple planes. These types of events are likely to be detected even with conventional 2D imaging approaches. Each frame represents an average over 3 seconds of activity. **(C)** Inappropriate ROI selection may lead to underestimate the effect of TTX on astrocyte Ca^{2+} activity (the "dilution" problem). *Top*: traces show that TTX effectively blocks the Ca^{2+} activity evoked by small axonal stimuli when the ROI is confined to the identified responding parts of the astrocyte. *Bottom*: when the size of the selected ROI is larger, e.g., comprising all the GCaMP6f-positive regions of the astrocyte, the result is that the stimulus-related, TTX-sensitive component is "diluted" in the stimulus-unrelated endogenous activity of the astrocyte, resulting in an apparent full lack of TTX-sensitivity (for further discussion see Text S1).

Supplemental Text S1. A controversial issue: TTX-sensitivity of basal Ca²⁺ activity in astrocytes

There is good evidence that Ca²⁺ activity in astrocytes starts at very early developmental stages (P2-P14), even before the establishment of mature neuronal connections and a fully functional circuitry. This early activity was reported by several studies to be TTX-insensitive, suggesting that it is intrinsically generated by the astrocytes, independently of neuronal firing (*42, 55, 56*). By P14 the intrinsic activity appears, however, to be significantly attenuated with respect to P4 (down to 20%, (*55*). On the other hand, in the course of the third postnatal week (P17-P21, (*57*)) and later on (P30-P40, (*14*)) some studies reported the presence of a TTX-sensitive component in the basal astrocytic Ca²⁺ activity. The latter observation was not, however, confirmed by other studies (*26, 39*), leaving the issue of TTX sensitivity uncertain. Observations made in the present study and further methodological considerations suggest that there can be explanations for these apparent contradictory reports.

The dilution problem
In this project, we tested the effect of TTX on: (a) basal Ca²⁺ activity in astrocytes from P30-40 hippocampal slices displaying sparse neuronal firing (*14*); (b) upon minimal axonal stimulation. At first glance, results of these two sets of experiments were inconsistent. Thus, while TTX mildly inhibited Ca²⁺ activity in astrocytic processes in basal condition (on average: -43.9 ± 13.4%, Fig 4B), it fully blocked the astrocytic Ca²⁺ response to minimal evoked neuronal activity in responding regions (Fig. 7B). Further analysis showed, however, that the mild effect did not correspond to a weak sensitivity of the basal Ca²⁺ activity to TTX. Instead, it revealed that sensitivity by different processes was different, with about half of them being strongly TTX-sensitive, and the other half only partially sensitive or not sensitive at all. This heterogeneity between different processes, which is likely present also more locally within individual processes, highlights a methodological issue that we can call the "dilution problem". This problem occurs when researches inadvertently associate in their measures TTX-sensitive and TTX-insensitive responses, thereby diluting the real, strong effect of TTX on only one component of the astrocyte Ca²⁺ activity. Depending on how the analysis is performed, the same problem can occur even when studying the Ca²⁺ activity induced in astrocytes by neuronal firing, which by definition has to be, and is, TTX-dependent (Fig. 7B,C). Thus, the astrocyte regions reliably responding to minimal evoked neuronal firing are small in size (about 0.5 % of the astrocyte volume). This makes them difficult to pinpoint in the bulk of the endogenous Ca²⁺ activity of the astrocyte, in the absence of any spatial and/or temporal cue (e.g. the position of the stimulated axon and/or the timing of stimulation). Fig. S11C exemplifies once again the "dilution problem" and shows the critical importance of correctly selecting the ROI containing the TTX-sensitive component. Thus, if the selected ROI does not correspond in size to the real responding region, but is wider, the TTX-sensitive component gets diluted in the TTX-insensitive one, with the dilution being proportional to the mismatch in size. As a result, the TTX effect appears to be smaller than really is (Fig. S11B). If the mismatch is big, it may eventually get fully undetected (Fig. S11C).

Other factors that may affect detection of a TTX-sensitive component of basal astrocytic Ca²⁺ activity in acute brain slice preparations
In addition to an intrinsic biological heterogeneity of the astrocytic Ca²⁺ activity, e.g., involving microdomains that are predominantly TTX-sensitive (loci of synaptic contacts, (*15*)) vs TTX-

insensitive (e.g, mitochondrial locations along processes, (*39*)), there can be additional experimental factors that may lead to detect more or less TTX-sensitive Ca^{2+} activity:

1) *Age of the animals and circuitry investigated in acute slice preparations.* As indicated above, the proportion of TTX-sensitive and TTX-insensitive astrocyte activity seems to be influenced by the developmental stage, and therefore by the age of the animals from which acute slice preparations are made. Moreover, the type of circuit investigated is relevant. Certain brain areas are denervated by slice preparation, paradoxically resulting in sPSC frequency being equal to mPSC frequency in TTX. This situation is seen for instance in the cerebellar cortex (*58, 59*) and is likely present also in cortical slices with e.g. transected thalamic afferents. In contrast, in horizontal hippocampal slices, where some connectivity between spontaneously active EC and DG is preserved, we experimentally verified that TTX application reduces sEPSC frequency by 30-50% (*14, 60*), which makes this area a suitable target for studying the TTX effect in astrocytes.

2) *Location of the astrocyte recordings in the slice preparation.* Cells in slices can exhibit a large heterogeneity due to variability in their microenvironment. Again, this can be biological variability, but also "experimental" variability. A predominant factor is the slicing process itself. For instance, some astrocytes (or parts of them) may have more of their axonal inputs transected than others and may therefore be less sensitive to TTX. Logically, astrocytes located closer to the slice surface are likely to be in this situation. Astrocytes on the surface may also experience lower levels of transmitters, factors, or ions (K^+) due to washout/interchange with the bath aCSF. On the other hand, astrocytes (or their processes) located deeper in the slice can be surrounded by a more anoxic tissue that may have different functional properties and metabolic requirements compared to more oxygenated layers of the slice.

3) *Properties of the Ca^{2+} indicators.* Another aspect requiring consideration is the suitability of the Ca^{2+} indicators used in assessing the TTX-sensitive component of basal astrocytic Ca^{2+} activity. Indicators with low SNR, including first generation GECIs (GCaMP3), may under-report some of the smaller/faster Ca^{2+} events, among which could be those associated with low-level neuronal activity. This is particularly true of membrane-bound GECI, which will also tend to over-buffer small events due to very high concentration at the plasma membrane in small compartments.

Supplemental Movie Captions: S1-S4

Movie S1

Comparative morphology of an astrocyte in 3D vs 2D.

Movie S2

Comparison of Ca^{2+} activity observable in 3D vs 2D.

Movie S3

Ca^{2+} imaging of astrocytes in vivo in awake mouse.

Movie S4

Axon-astrocyte morphological interactions in 3D vs 2D.

Supplemental References 43-60:

43. P. G. Hirrlinger, A. Scheller, C. Braun, J. Hirrlinger, F. Kirchhoff, Temporal control of gene recombination in astrocytes by transgenic expression of the tamoxifen-inducible DNA recombinase variant CreERT2. *Glia* **54**, 11-20 (2006).

44. C. Nolte *et al.*, GFAP promoter-controlled EGFP-expressing transgenic mice: a tool to visualize astrocytes and astrogliosis in living brain tissue. *Glia* **33**, 72-86 (2001).

45. S. Habbas *et al.*, Neuroinflammatory TNFalpha Impairs Memory via Astrocyte Signaling. *Cell* **163**, 1730-1741 (2015).

46. J. Ding, A. F. Luo, L. Hu, D. Wang, F. Shao, Structural basis of the ultrasensitive calcium indicator GCaMP6. *Science China. Life sciences* **57**, 269-274 (2014).

47. A. Nimmerjahn, F. Kirchhoff, J. N. Kerr, F. Helmchen, Sulforhodamine 101 as a specific marker of astroglia in the neocortex in vivo. *Nature methods* **1**, 31-37 (2004).

48. C. Schnell, Y. Hagos, S. Hulsmann, Active sulforhodamine 101 uptake into hippocampal astrocytes. *PloS one* **7**, e49398 (2012).

49. A. Holtmaat *et al.*, Long-term, high-resolution imaging in the mouse neocortex through a chronic cranial window. *Nature protocols* **4**, 1128-1144 (2009).

50. K. Masamoto *et al.*, Repeated longitudinal in vivo imaging of neuro-glio-vascular unit at the peripheral boundary of ischemia in mouse cerebral cortex. *Neuroscience* **212**, 190-200 (2012).

51. N. Medvedev *et al.*, Glia selectively approach synapses on thin dendritic spines. *Philosophical transactions of the Royal Society of London. Series B, Biological sciences* **369**, 20140047 (2014).

52. B. K. Andrasfalvy *et al.*, Quantum dot-based multiphoton fluorescent pipettes for targeted neuronal electrophysiology. *Nature methods* **11**, 1237-1241 (2014).

53. M. Raastad, Extracellular activation of unitary excitatory synapses between hippocampal CA3 and CA1 pyramidal cells. *The European journal of neuroscience* **7**, 1882-1888 (1995).

54. E. Meijering *et al.*, Design and validation of a tool for neurite tracing and analysis in fluorescence microscopy images. *Cytometry. Part A : the journal of the International Society for Analytical Cytology* **58**, 167-176 (2004).

55. H. R. Parri, T. M. Gould, V. Crunelli, Spontaneous astrocytic Ca2+ oscillations in situ drive NMDAR-mediated neuronal excitation. *Nature neuroscience* **4**, 803-812 (2001).

56. F. Aguado, J. F. Espinosa-Parrilla, M. A. Carmona, E. Soriano, Neuronal activity regulates correlated network properties of spontaneous calcium transients in astrocytes in situ. *The Journal of neuroscience : the official journal of the Society for Neuroscience* **22**, 9430-9444 (2002).

57. E. Barat *et al.*, Subthalamic nucleus electrical stimulation modulates calcium activity of nigral astrocytes. *PloS one* **7**, e41793 (2012).

58. I. Savtchouk, S. J. Liu, Remodeling of synaptic AMPA receptor subtype alters the probability and pattern of action potential firing. *The Journal of neuroscience : the official journal of the Society for Neuroscience* **31**, 501-511 (2011).

59. I. Savtchouk *et al.*, Topological Regulation of Synaptic AMPA Receptor Expression by the RNA-Binding Protein CPEB3. *Cell reports* **17**, 86-103 (2016).

60. P. Jourdain *et al.*, Glutamate exocytosis from astrocytes controls synaptic strength. *Nature neuroscience* **10**, 331-339 (2007).